ADVANCED FUNCTIONAL MATERIALS
www.afm-journal.de



# Molecular Engineering to Tune the Ligand Environment of Atomically Dispersed Nickel for Efficient Alcohol Electrochemical Oxidation

*Zhifu Liang, Daochuan Jiang, Xiang Wang, Mohsen Shakouri, Ting Zhang, Zhongjun Li, Pengyi Tang,* Jordi Llorca, Lijia Liu,* Yupeng Yuan, Marc Heggen, Rafal E. Dunin-Borkowski, Joan R. Morante, Andreu Cabot,* and Jordi Arbiol**

**Atomically dispersed metals maximize the number of catalytic sites and enhance their activity. However, their challenging synthesis and characterization strongly complicates their optimization. Here, the aim is to demonstrate that tuning the electronic environment of atomically dispersed metal catalysts through the modification of their edge coordination is an effective strategy to maximize their performance. This article focuses on optimizing nickel-based electrocatalysts toward alcohol electrooxidation in alkaline solution. A new organic framework with atomically dispersed nickel is first developed. The coordination environment of nickel within this framework is modified through the addition of carbonyl (C=O) groups. The authors then demonstrate that such nickel-based organic frameworks, combined with carbon nanotubes, exhibit outstanding catalytic activity and durability toward the oxidation of methanol ($CH_3OH$), ethanol ($CH_3CH_2OH$), and benzyl alcohol ($C_6H_5CH_2OH$); the smaller molecule exhibits higher catalytic performance. These outstanding electrocatalytic activities for alcohol electrooxidation are attributed to the presence of the carbonyl group in the ligand chemical environment, which enhances the adsorption for alcohol, as revealed by density functional theory calculations. The work not only introduces a new atomically dispersed Ni-based catalyst, but also demonstrates a new strategy for designing and engineering high-performance catalysts through the tuning of their chemical environment.**

## 1. Introduction

The electrochemical oxidation of alcohols is at the basis of several strategic chemical processes and energy technologies, including electrochemical organic synthesis, biomass, and organic waste valorization, and direct alcohol fuel cells (DAFC).[1] The electrooxidation of alcohols offer numerous advantages over competing valorization strategies and energy technologies, such as high energy densities and energy conversion efficiency, operation/reaction at low working temperature with high selectivity, and low fuel cost with easy production, transportation, and storage.[1] However, despite their numerous advantages, the deployment of electrocatalytic valorization strategies and DAFCs is hampered by their low cost-effectiveness in large part associated with the use of moderately efficient catalysts based on high-cost and low-abundance elements such as platinum and palladium.[2,3] Besides, current alcohol electrooxidation catalysts become rapidly poisoned with carbon monoxide,

Z. F. Liang, T. Zhang, J. Arbiol
Catalan Institute of Nanoscience and Nanotechnology (ICN2)
CSIC and BIST
Campus UAB, Bellaterra, Barcelona, Catalonia 08193, Spain
E-mail: arbiol@icrea.cat

Z. F. Liang, X. Wang, A. Cabot, J.R. Morante
Functional Nanomaterials Group
Catalonia Institute for Energy Research – IREC
Sant Adrià de Besòs, Barcelona Catalonia 08930, Spain
E-mail: acabot@irec.cat

The ORCID identification number(s) for the author(s) of this article can be found under https://doi.org/10.1002/adfm.202106349.



**DOI: 10.1002/adfm.202106349**

D. Jiang, Y. Yuan
School of Chemistry and Chemical Engineering
Anhui University
Heifei Anhui 230601, China

M. Shakouri
Canadian Light Source
Saskatoon S7N 0X4, Canada

Z. J. Li
School of Physics
Hefei University of Technology
Hefei 230009, P. R. China

P. Y. Tang
State Key Laboratory of Information Functional Materials, 2020 X-Lab
Shanghai Institute of Microsystem and Information Technology
Chinese Academy of Sciences
Shanghai 200050, China
E-mail: py.tang@mail.sim.ac.cn

which further limits their cost-effectiveness. Thus, the development of efficient and stable alcohol oxidation electrocatalysts based on abundant elements is a topic of major interest.

Several non-precious transition metal catalysts have been proposed for alcohol electro-oxidation.[4,5] Among them, nickel-based catalysts are considered the most promising candidates owing to their high catalytic activity, low price, and notable abundance. Numerous Ni-based catalysts, such as $Ni_{0.75}Cu_{0.25}$,[6] NiSn alloy,[7] $Ni_{93}Bi_7$,[8] NiSe,[9] NiO,[10] and metal–organic frameworks with $Ni(OH)_4$,[11] and Ni-Co hydroxide[12] have been developed and tested for alcohol electrochemical-oxidation. However, the reported onset potentials and stabilities are still not fully satisfactory, which calls for novel strategies to design and engineer nickel-based catalysts with improved performance.

Recently, 2D covalent organic frameworks and metal–organic frameworks (MOF) with highly tunable pore structure and functionality, and high density of active sites, have arisen broad interest as electrocatalysts.[13] Optimized electrocatalysts based on such 2D structures have demonstrated outstanding performances toward oxygen evolution and reduction,[14,15] and carbon dioxide reduction.[16,17] However, despite their high potential for alcohol electrooxidation, these 2D materials and particularly a nickel-containing 2D organic framework have yet to be developed and optimized toward this electrocatalytic reaction.

Here, we report the synthesis of an atomically-dispersed nickel 2D molecular organic framework containing abundant carbonyl (C=O) functional groups within the nickel ion coordination environment. Its atomic structure and how the outstanding electrocatalytic activities and durabilities obtained for the electrochemical-oxidation of methanol, ethanol, and benzyl alcohol were analyzed, are related to the alcohol adsorption ability of the carbonyl functional groups and the high unsaturated coordination number of the nickel ions within the new catalyst presented here.

## 2. Results and Discussion

The nickel-based 2D organic framework with abundant carbonyl functional groups (Ni–2D–O–SA) was solvothermally synthesized through a Schiff-based reaction between 2,5-hydroxyterephthalaldehyde (HBC) (Scheme S1, Supporting Information) and tetramino-benzoquinone (TABQ) (Scheme S2, Supporting Information) in *N*-methyl-2-pyrrolidone (NMP) (see details in **Figure 1**a; Scheme S3, Supporting Information). The dark-black color of the obtained solid indicated the formation of a conjugated polymer, which was washed by water and methanol to remove low molecular mass impurities, and then dried under vacuum. For comparison, a reference nickel-based 2D organic framework without carbonyl chemical groups (Ni–2D–SA) was prepared under the same reaction condition but using 1,2,4,5-benzenetetraamine tetrahydrochloride (TAB) instead of TABQ (Scheme S4, Supporting Information).[18]

Scanning electron microscopy (SEM) images (Figure S1a,b, Supporting Information) show that the Ni–2D–O–SA sample has a cotton-like morphology. The X-ray diffraction (XRD) pattern (Figure S3, Supporting Information) of the Ni–2D–O–SA powder was similar to that of graphite, with a diffraction peak at 26.29° corresponding to the (001) family planes and which indicated $\pi$–$\pi$ layered stacking.[19] In contrast to the clear crystalline and layered structure displayed by Ni–2D–O–SA, the XRD pattern of Ni–D–SA displayed a much broader and less intense peak at around 26°. This result indicates that the introduction of carbonyl groups enhances the crystallinity of the nickel-based 2D organic framework used here.

Fourier transform infrared (FT-IR) spectroscopy was used to evaluate the chemical structure of the samples (Figure S4, Supporting Information). Based on the FT-IR spectra, the signal for C=N appeared at 1642 $cm^{-1}$ for Ni–2D–SA, and 1648 $cm^{-1}$ for Ni–2D–O–SA. The vibration of the carbonyl bond (C=O) in Ni–2D–O–SA negatively shifted below 1600 $cm^{-1}$ and overlapped with other vibrations. For Ni–2D–O–SA, the vibration peak for the C−(C=O)−C bond, which is a footprint of TABQ, shifted from 1140 to 1010 $cm^{-1}$ due to the coordination effect and the attraction between the layers. This result already points out to the successful introduction of the carbonyl groups in the organic framework.[20]

The survey X-ray photoelectron spectroscopy (XPS) spectra revealed the sole presence of C, N, Ni, and O in both samples (Figures S5 and S6, Supporting Information).[21] For both samples, the high-resolution Ni 2p spectrum showed a unique doublet at binding energies of 856 eV (Ni $2p_{3/2}$) and 873.3 eV (Ni $2p_{1/2}$), significantly above those of NiO.[22,23]

The local environment in Ni–2D–O–SA was further analyzed and compared with that of NiO using X-ray absorption fine structure (XAFS) at the Ni K-edge (Figure 1b–d; Figure S7, Supporting Information). Comparing the spectral features at the near-edge, that is, the X-ray absorption near-edge structure (XANES), we observe the absorption onset of Ni–2D–O–SA at slightly lower energy than that of NiO (Figure 1b). Differences are more clearly seen when plotting the first derivative of the two spectras (Figure S7a, Supporting Information), as shown in the inset of **Figure 2**b. Besides, the main absorption peak of Ni–2D–O–SA has a lower intensity than that of NiO. Both features indicate that compared with NiO, where Ni is fully surrounded by O, within Ni–2D–O–SA, Ni atoms are partially surrounded by a lower electronegativity element, that is, N. A more quantitative picture was obtained by analyzing the extended XAFS (EXAFS) features. The fitting of the Fourier transformed EXAFS spectrum suggests that Ni is coordinated with two N atoms and two O atoms, at a bond length 1.87 and 2.05 Å,

P. Y. Tang, M. Heggen, R. E. Dunin-Borkowski
Ernst Ruska-Centre for Microscopy and Spectroscopy with Electrons and Peter Grünberg Institute, Forschungszentrum Jülich GmbH
52425 Jülich, Germany
J. Llorca
Institute of Energy Technologies
Department of Chemical Engineering and Barcelona Research Center in Multiscale Science and Engineering
Universitat Politècnica de Catalunya
EEBE
Barcelona Catalonia 08019, Spain
L. Liu
Department of Chemistry
Western University
1151 Richmond Street, London ON N6A5B7, Canada
E-mail: lijia.liu@uwo.ca
A. Cabot, J. Arbiol
ICREA
Pg. Lluís Companys 23, Barcelona Catalonia 08010, Spain

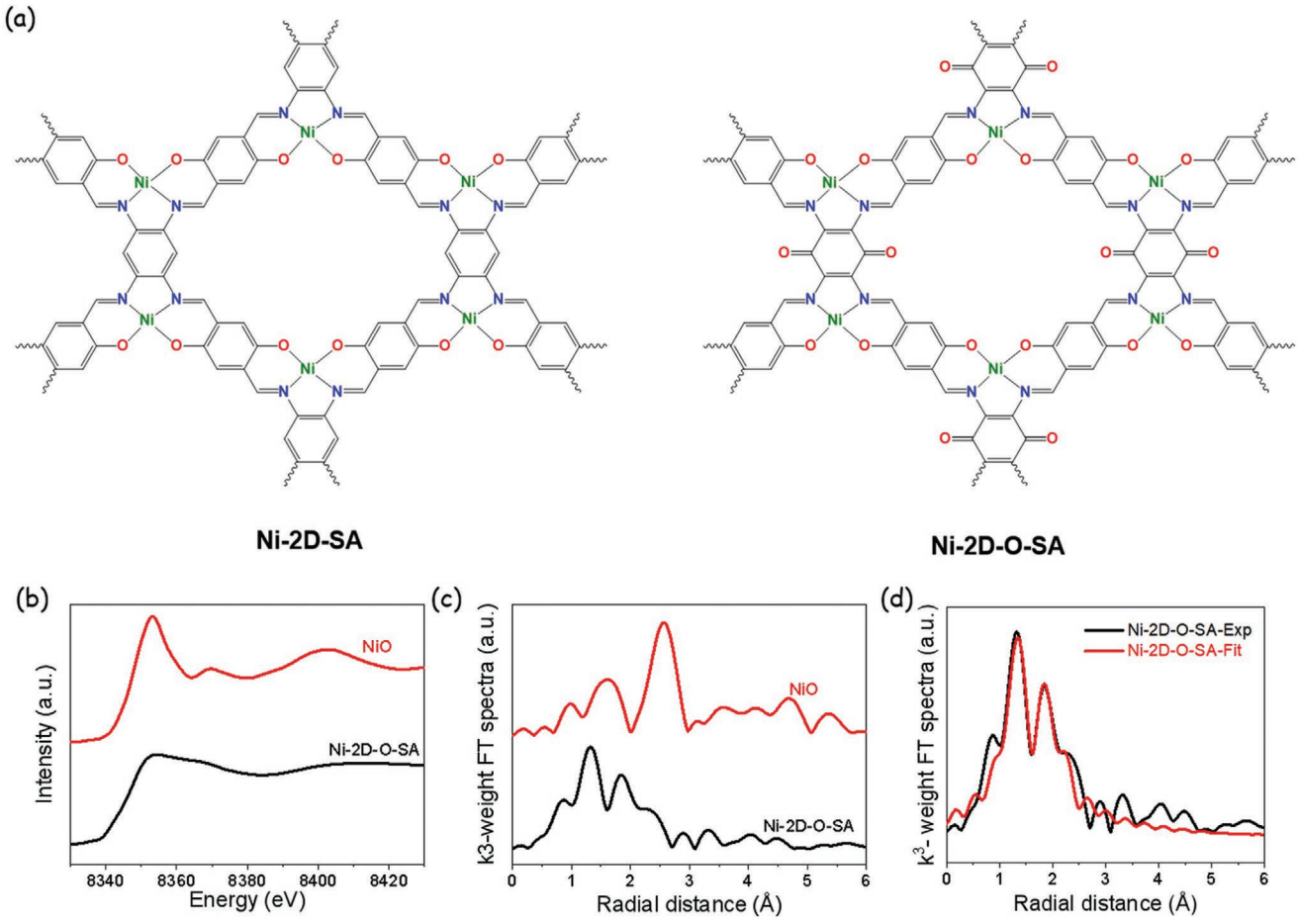


**Figure 1.** a) Scheme of the synthesis procedure used to produce Ni–2D–O–SA. b) Ni K-edge XANES spectrum of Ni–2D–O–SA compared with a commercial NiO powder. c) Fourier transformed Ni K-edge EXAFS spectra of Ni–2D–O–SA and NiO plotted in R-space. d) Fitting of the Fourier transformed EXAFS spectrum in R-space of Ni–2D–O–SA.

respectively (Figure 1c,d).[24] The contribution at longer radial distances comes from C atoms with a coordination number of 6 and a bond length of 2.65 Å. The detailed fitting parameters can be found in Table S1, Supporting Information. Overall, XAFS analysis provided strong evidence of the formation of the $NiN_2O_2$ salophen structure unit in the Ni–2D–O–SA framework.

High angle annular dark-field (HAADF) aberration-corrected scanning transmission electron microscopy (STEM) was used to analyse the nickel dispersion. As shown in Figure 2a–c; Figure S8a–c, Supporting Information, Ni–2D–O–SA contained a high density of isolated and homogeneously distributed nickel atoms. The uniform distribution of Ni, C, N, and O was further confirmed by energy-dispersed X-ray spectroscopy (EDS) elemental mapping (Figure 2d).

The surface area of Ni–2D–O–SA and Ni–2D–SA, evaluated from $N_2$ adsorption–desorption isotherms at 77 K (Figure S9, Supporting Information) using the Brunauer–Emmett–Teller equation was 21.1 and 83 $m^2\ g^{-1}$, respectively. Thus, the introduction of carbonyl functional groups significantly decreased the surface area of the material, which we associate with an enhancement of the layer–layer interaction that results in slightly more densely packed frameworks.

To improve the electrical conductivity of these nickel-based organic frameworks, as required to apply them as electrocatalysts, they were loaded on multi-wall carbon nanotubes (CNT) through the $\pi$–$\pi$ packing interaction. The XRD patterns of the obtained Ni–2D–O–SA–CNT and Ni–2D–SA–CNT composites, showed a unique peak at ≈26° (Figure S10, Supporting Information), which was assigned to the overlap between the CNT and the organic framework structures. SEM (Figure S1c,d, Supporting Information), STEM images, and EDX compositional maps (Figure S11, Supporting Information) showed the composites morphology and confirmed the homogeneous loading of Ni–2D–O–SA on the CNTs.

**Figure 3**a exhibits the cyclic voltammograms (CV) of the two samples in the range from 0 to 0.65 V in 1.0 M KOH electrolyte with a scan rate of 50 mV $s^{-1}$. The anodic peak at 0.50 V versus Hg/HgO measured in the forward scan with Ni–2D–O–SA–CNT is attributed to $Ni^{2+}$ oxidation, and the cathodic peak in the backward scan at 0.38 V corresponds to the reduction of $Ni^{3+}$ species. For Ni–2D–SA–CNT, the anodic peak shifted to 0.54 V and the cathodic peak to 0.42 V. The current density at the $Ni^{2+}$ oxidation peak in the Ni–2D–O–SA–CNT electrocatalyst was 19 mA $cm^{-2}$, which is ≈9.5 times higher than that of Ni–2D–SA–CNT, 2 mA $cm^{-2}$. These results indicate a much higher electrochemical activity of the Ni ions within Ni–2D–O–SA–CNT and their easier oxidation to $Ni^{3+}$. Besides, the ratio between the anodic and the cathodic peak current

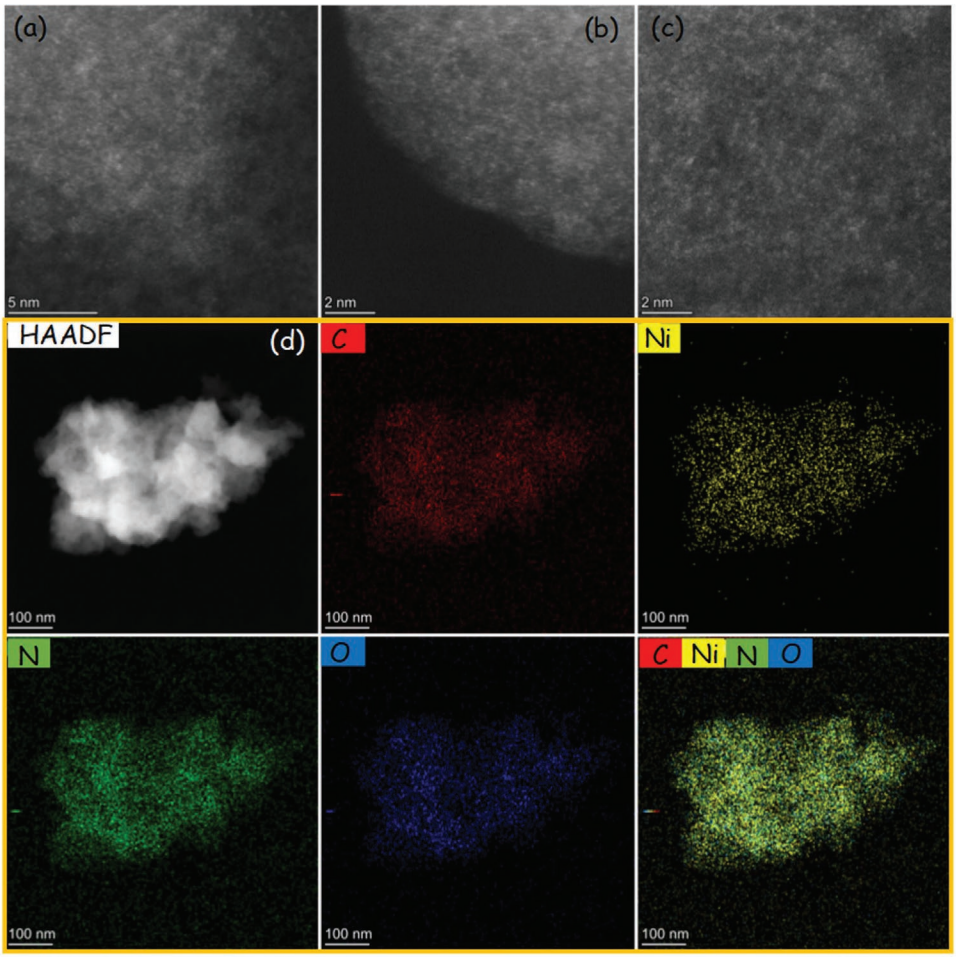


**Figure 2.** a–c) HAADF–STEM images of Ni–2D–O–SA displaying the presence of atomically dispersed nickel atoms. d) Low magnification HAADF–STEM image and EDS elemental mapping.

densities was close to 1 for both catalysts, indicating a reversible $Ni^{2+}/Ni^{3+}$ redox reaction in both materials.[25]

CV of the reduction/oxidation process allowed to estimate the surface coverage (Γ) of $Ni^{2+}/Ni^{3+}$ within Ni–2D–O–SA–CNT to be $1.32 \times 10^{-7}$ mol $cm^{-2}$, two orders of magnitude above that of Ni–2D–SA–CNT, $5.17 \times 10^{-9}$ mol $cm^{-2}$ (Figure 3a; Equation (S1), Supporting information).[26] Figure 3b; Figure S12, Supporting Information, display CV curves at different scan rates, from 10 to 100 mV $s^{-1}$, obtained with these two catalysts in 1.0 M KOH electrolyte. The variation of the anodic and cathodic peak current densities with the square root of the voltage scan rate was linearly fitted with $R^2 > 0.99$ for both samples (Figure S12, Supporting Information), demonstrating the $Ni^{2+}/Ni^{3+}$ redox reaction to be diffusion limited.[25] From this dependence, an apparent diffusion coefficient $D'$ was evaluated (see Equation S3, Supporting Information). The $D'$ obtained with Ni–2D–O–SA–CNT is $2.3 \times 10^{-6}$ g $cm^{-1}$ $s^{-1}$, which is close to an order of magnitude higher than with Ni–2D–SA–CNT, $3.3 \times 10^{-7}$ g $cm^{-1}$ $s^{-1}$.

The alcohol electrooxidation performance of Ni–2D–O–SA–CNT and Ni–2D–SA–CNT electrocatalysts was analyzed by linear sweep voltammetry (LSV) in 1 M KOH and 1 M KOH + 1 M methanol solutions using a conventional three-electrode setup (Figure 3c,d). The OER activity of Ni–2D–O–SA–CNT was just slightly improved compared to that of Ni–2D–SA–CNT. However, the Ni–2D–O–SA–CNT catalysts showed much higher activity toward methanol oxidation reaction (MOR), with current densities increasing from 31 to 106 mA $cm^{-2}$ in the range 0.5–0.6 V versus Hg/HgO, that is, six-fold higher current densities compared with Ni–2D–SA–CNT. Thus, the introduction of the carbonyl group (C=O) at the ligand environment of the dispersed Ni-atoms active sites clearly results in much higher MOR catalytic activities.

The charge transfer resistances of these two catalysts were evaluated through electrochemical impedance spectroscopy (EIS). The EIS Nyquist plot of Ni–2D–O–SA–CNT (Figure 3e) presents a smaller semicircle than Ni–2D–SA–CNT at 0.56 V in 1 M KOH + 1 M methanol electrolyte, denoting a lower charge transfer resistance ($R_3$) and thus faster MOR kinetics.[27] On the other hand, the charge transfer resistance for OER of Ni–2D–O–SA–CNT is similar to that of Ni–2D–SA–CNT at 0.67 V (Figure S13, Supporting Information), which is consistent with the similar OER activities of these two catalysts.

As shown in the chronopotentiometry (CP) curve (Figure 3f), the Ni–2D–O–SA–CNT electrocatalyst maintained constant current densities of 10 and 30 mA $cm^{-2}$ for 12 h without a

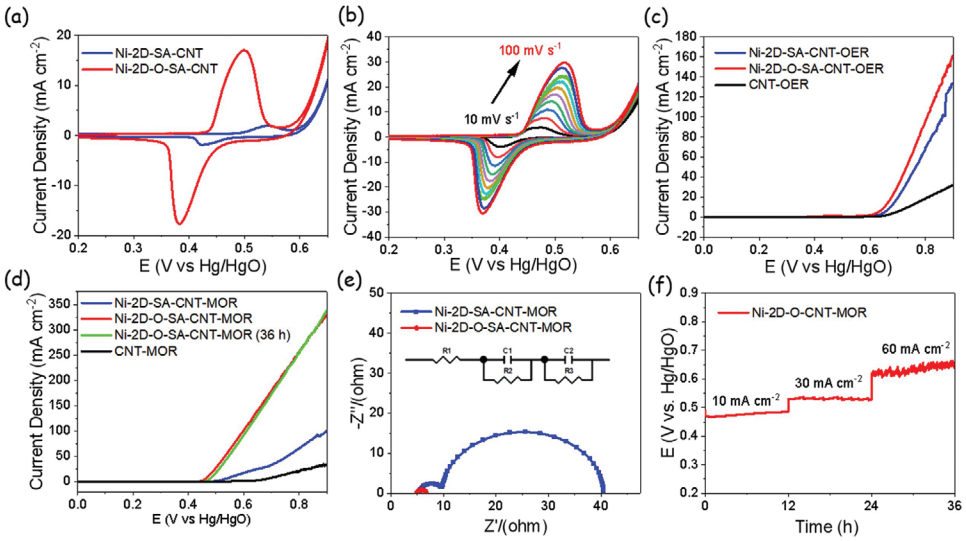


**Figure 3.** a) CV of Ni–2D–O–SA–CNT and Ni–2D–SA–CNT electrocatalysts in 1 M KOH at 50 mV $s^{-1}$ potential sweep rate. b) CVs of Ni–2D–O–SA–CNT electrocatalysts in 1 M KOH obtained at an increasing potential sweep rate, from 10 to 100 mV $s^{-1}$. c,d) LSV curves obtained with Ni–2D–SA–CNT, Ni–2D–O–SA–CNT, and reference carbon nanotubes (CNTs) catalysts in 1.0 M KOH (c) and 1 M KOH + 1 M methanol in the potential range 0 to 0.9 V versus Hg/HgO at a scan rate of 5 mV $s^{-1}$ (d). e) EIS Nyquist plots at 0.56 V in 1 M KOH + 1 M methanol solution. f) CP long-term stability of Ni–2D–O–SA–CNT at 10, 30, and 60 mA $cm^{-2}$. No iR compensation was applied to the displayed data.

significant increase in the required potential. When increasing the current density to 60 mA $cm^{-2}$, the potential raised ≈4.8% during 12 h, which is attributed to the methanol consumption. After 36 h chronopotentiometry test, LSV curves recorded with the used electrocatalysts in a fresh 1 M KOH + 1 M methanol electrolyte (Figure 3d) showed almost no variation with respect to those obtained with the fresh electrocatalysts, what demonstrates the excellent stability of Ni–2D–O–SA–CNT during MOR. After the stability test, the pH value of the solution is 14.12, which is not a significant change compared to the initial solution (pH = 14).

The XRD pattern of Ni–2D–O–SA–CNT after MOR (Figure S14, Supporting Information) displayed no significant variation with respect to the sample before the electrochemical tests, which confirmed the excellent structural stability of the 2D material and the growth of no additional crystalline phase of the nickel or nickel oxide nanoparticles during the reaction, indicating there is no agglomeration of nickel atom active sites.

Methanol adsorption is the initial and a limiting step in MOR. To understand the contribution of C=O groups to methanol adsorption, density functional theory (DFT) calculations were carried out. Selected fragments were shown in Figure S15, Supporting Information. **Figure 4** shows the optimal methanol adsorption configurations on top of a Ni site in both Ni–2D–SA and Ni–2D–O–SA. The adsorption energy is –0.248 eV and –0.225 eV in Ni–2D–SA and Ni–2D–O–SA, respectively. The negative adsorption energies suggest that methanol adsorption is thermodynamically favored in both cases. Interestingly, the adsorption distance (*d*) between the O atom of methanol and Ni in Ni–2D–O–SA is 3.11 Å, which is shorter than in Ni–2D–SA (3.27 Å). Compared with Ni–2D–SA, the 10% lower adsorption energy and 5% shorter adsorption distance indicate a more effective adsorption of the methanol molecule on the surface of Ni–2D–O–SA. What is more, upon adsorption, the H—O—$CH_3$ angle in Ni–2D–O–SA increases from 108.25° to 109.04°, while the H—O—$CH_3$ angle in Ni–2D–SA remains almost unchanged after optimization. This result indicates that Ni–2D–O–SA can facilitate the activation of the methanol molecule. We also identify the O of the C=O group as a methanol adsorption site. DFT calculations show that the methanol molecule tends to adsorb at such O site with the OH group in methanol parallel to the surface. The shortest distance between the methanol molecule and the surface is 1.87 Å, which is much smaller than in the Ni–2D–SA surface (2.5 Å). Thus, based on the DFT calculations, it is reasonable to conclude that the addition of carbonyl (C=O) groups to the organic framework results in more effective adsorption as well as activation of the methanol molecule, which explains the higher activity of Ni–2D–O–SA toward MOR when compared with Ni–2D–SA.

Beyond MOR, we also examined the electrocatalytic activity of the produced catalysts toward the oxidation of other alcohols. Compared with Ni–2D–SA–CNT, Ni–2D–O–SA–CNT presented significantly higher electrocatalytic performance toward the electrochemical oxidation of both ethanol (EOR) (**Figure 5**a) and benzyl alcohol (BOR) (Figure 5b). Especially for the BOR, the current density at 0.6 V obtained with Ni–2D–O–SA–CNT was ≈77 mA $cm^{-2}$, which is ≈eight times higher than that of Ni–2D–SA–CNT (9.7 mA $cm^{-2}$).

CP measurements were used to test the stability of Ni–2D–O–SA–CNT for EOR. As shown in Figure S16, Supporting Information, Ni–2D–SA–CNT exhibited excellent long-term stability for EOR, similar to that obtained for MOR. For BOR, chronoamperometric measurements (Figure S17, Supporting Information) show the current density decay associated with the consumption of benzyl alcohol. Notice in this respect that the initial concentration of benzyl alcohol was just 0.1 M, since the steric hindrance of benzene may prevent an efficient

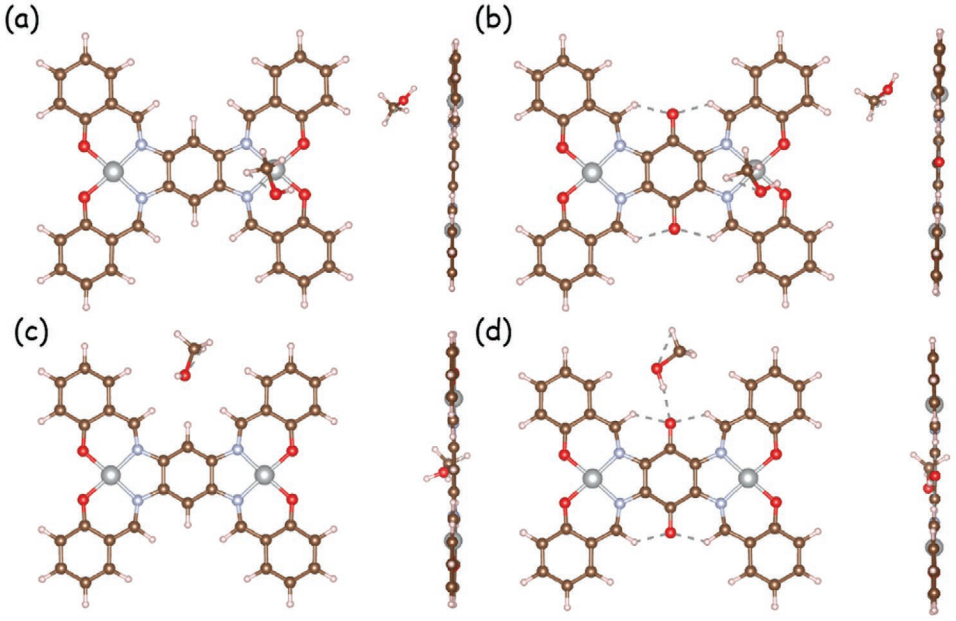


**Figure 4.** a,b) Optimal methanol adsorption configurations on top of the Ni site in both Ni–2D–SA (a) and Ni–2D–O–SA (b). c,d) Optimal methanol adsorption configurations on top of the carbonyl site in both Ni–2D–SA (c) and Ni–2D–O–SA (d) (red is oxygen, light blue is nitrogen, grey is nickel, brown is carbon).

reaction at higher concentrations. The EIS spectra for EOR and BOR were similar to those obtained for MOR, confirming that Ni–2D–O–SA–CNT is also characterized by a highly efficient charge transfer and a highly favorable EOR and BOR kinetics (Figure S18, Supporting Information).

Finally, in order to confirm the product of the electrochemical oxidation of alcohol, nuclear magnetic resonance (NMR) tests were conducted to analyze the associated products of electrochemical oxidation of alcohol. As shown in Figure S19, Supporting Information, the NMR spectrum after the MOR stability test displays the characteristic chemical shift of $HCOO^-$ at 8.33 ppm, while the characteristic chemical shift of HCHO in the range of ≈9–10 ppm was not observed, demonstrating that the final product of methanol oxidation is formate ($HCOO^-$). Furthermore, the NMR spectrum (Figure S20, Supporting Information) of the products from benzyl alcohol oxidation showed a chemical shift in the range of ≈7–8 ppm, which is assigned to the characteristic chemical shift of the proton in the benzene ring of benzoate. The characteristic chemical shift belonging to the aldehyde (−CHO) of benzaldehyde was not observed at the range of ≈9–10 ppm, demonstrating that the final product of the benzyl alcohol oxidation was benzoate ($C_6H_5COO^-$). The NMR spectra of the EOR electrolyte did also not display the characteristic chemical shift of the aldehyde (−CHO). The characteristic chemical shift of $CH_3COO^-$ appears at 1.83 ppm (Figure S21, Supporting Information).

Taking into account the above NMR results, we propose the following electrochemical reaction for the alcohol electrochemical oxidation (**Figure 6**):

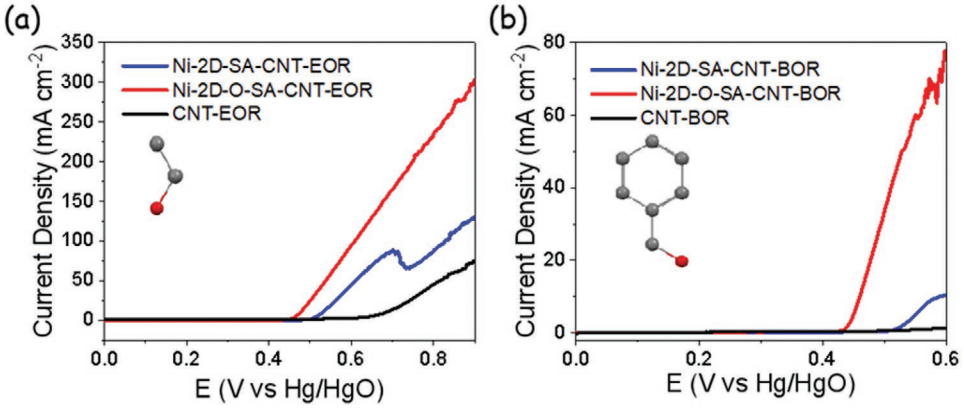


**Figure 5.** a) LSV of Ni–2D–SA–CNT, Ni–2D–O–SA–CNT, and CNT in 1 M KOH+1 M methanol from 0 to 0.9 V versus Hg/HgO at a scan rate of 5 mV $s^{-1}$. b) LSV of Ni–2D–SA–CNT, Ni–2D–O–SA–CNT, and the CNT in 1 M KOH + 0.1 M benzyl alcohol from 0 to 0.9 V versus Hg/HgO at a scan rate of 5 mV $s^{-1}$.

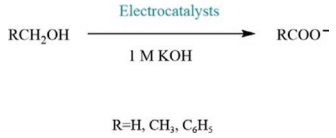


**Figure 6.** Scheme of the electrochemical oxidation reaction of alcohol.

## 3. Conclusion

In conclusion, we detailed the synthesis of a new nickel-based 2D organic framework and proposed a facile molecular engineering strategy to tune the ligand coordination environments of nickel ion centers. Through this strategy, carbonyl (C=O) groups were introduced and proved to decisively contribute to an efficient alcohol electro-oxidation in alkaline solution. EXAFS and XANES analysis confirmed the Ni salophen unit structure, $NiN_2O_2$, within the 2D organic frameworks. The atomically dispersed nickel within a framework containing the carbonyl groups displayed outstanding MOR, EOR, and BOR performance. DFT calculations suggested that the introduction of the C=O functional groups favor the absorption and activation of methanol molecules, which is at the origin of the improved MOR observed. The present work not only offers novel materials and a promising strategy to design more efficient atomically dispersed nickel-based catalysts for alcohol oxidation, but it could also benefit other research fields related to electrochemical-organic synthesis, energy conversion and storage.

## Supporting Information

Supporting Information is available from the Wiley Online Library or from the author.

## Acknowledgements

Z.F.L. and D.J. contributed equally to this work. ICN2 is supported by the Severo Ochoa program from Spanish MINECO (Grant No. SEV-2017-0706) and is funded by the CERCA Programme /Generalitat de Catalunya. Part of the present work has been performed in the framework of Universitat Autònoma de Barcelona Materials Science Ph.D. program. Z.L. acknowledges funding from MINECO SO-FPT Ph.D. grant (SEV-2013-0295-17-1). This project has received funding from the European Union's Horizon 2020 research and innovation program under grant agreement No 823717-ESTEEM3. The present work is supported by the European Regional Development Fund and by the Spanish MINECO through the projects ENE2016-77798-C4-3-R, ENE2017-85087-C3, and project NANOGEN (PID2020-116093RB-C43). X.W. and T.Z. thank the China Scholarship Council for the scholarship support. P. Tang acknowledges the Humboldt Research Fellowship. Authors acknowledge funding from Generalitat de Catalunya 2017SGR327 and 2017SGR1246. L.L. acknowledges the support from Natural Sciences and Engineering Research Council of Canada (NSERC, DG RGPIN-2020-06675). J.L. is a Serra Húnter Fellow and is grateful to MICINN/FEDER RTI2018-093996-B-C31, GC 2017 SGR 128, and to ICREA Academia program. XAS measurements were performed at the Canadian Light Source, a national research facility at the University of Saskatchewan, which is supported by the Canada Foundation for Innovation (CFI), the Natural Sciences and Engineering Research Council (NSERC), the National Research Council (NRC), the Canadian Institutes of Health Research (CIHR), the Government of Saskatchewan, and the University of Saskatchewan.

## Conflict of interest

The authors declare no conflict of interest.

## Data Availability Statement

Research data are not shared.

## Keywords

alcohol oxidation, atomically dispersed metals, electrocatalytic oxidation, nickel, 2D organic frameworks

Received: July 2, 2021
Revised: August 12, 2021
Published online:

[1] a) E. Antolini, E. R. Gonzalez, *J. Power Sources* **2010**, *195*, 3431; b) K. C. Cheung, W. L. Wong, D. L. Ma, T. S. Lai, K. Y. Wong, *Coord. Chem. Rev.* **2007**, *251*, 2367; c) D. P. Hickey, M. S. McCammant, F. Giroud, M. S. Sigman, S. D. Minteer, *J. Am. Chem. Soc.* **2014**, *136*, 15917; d) N. Kakati, J. Maiti, S. H. Lee, B. Viswanathan, Y. S. Yoon, *Chem. Rev.* **2014**, *114*, 12397; e) R. Ciriminna, G. Palmisano, M. Pagliaro, *ChemCatChem* **2015**, *7*, 552.
[2] Y. Tong, X. Yan, J. Liang, S. X. Dou, *Small* **2021**, *17*, 1904126.
[3] M. A. F. Akhairi, S. K. Kamarudin, *Int. J. Hydrogen Energy* **2016**, *41*, 4214.
[4] a) S. Rezaee, S. Shahrokhian, *Appl. Catal., B* **2019**, *244*, 802; b) A. Badalyan, S. S. Stahl, *Nature* **2016**, *535*, 406.
[5] G. M. K. Tolba, N. A. M. Barakat, A. M. Bastaweesy, E. A. Ashour, W. Abdelmoez, M. H. El-Newehy, S. S. Al-Deyab, H. Y. Kim, *J. Mater. Sci. Technol.* **2015**, *31*, 97.
[6] X. Cui, P. Xiao, J. Wang, M. Zhou, W. Guo, Y. Yang, Y. He, Z. Wang, Y. Yang, Y. Zhang, Z. Lin, *Angew. Chem., Int. Ed.* **2017**, *56*, 4488.
[7] J. Li, Z. Luo, Y. Zuo, J. Liu, T. Zhang, P. Tang, J. Arbiol, J. Llorca, A. Cabot, *Appl. Catal., B* **2018**, *234*, 10.
[8] A. Dubale, Y. Zheng, H. Wang, R. Hübner, Y. Li, J. Yang, J. Zhang, N. Sethi, L. He, Z. Zheng, W. Liu, *Angew. Chem., Int. Ed.* **2020**, *132*, 13995.
[9] B. Zhao, J. Liu, C. Xu, R. Feng, P. Sui, L. Wang, J. Zhang, J. L. Luo, X. Z. Fu, *Adv. Funct. Mater.* **2020**, *31*, 2008812.
[10] C. Liu, W. Zhou, J. Zhang, Z. Chen, S. Liu, Y. Zhang, J. Yang, L. Xu, W. Hu, Y. Chen, Y. Deng, *Adv. Energy Mater.* **2020**, *10*, 2001397.
[11] Y. Wu, J. Tian, S. Liu, B. Li, J. Zhao, L. Ma, D. Li, Y. Lan, X. Bu, *Angew. Chem., Int. Ed.* **2019**, *58*, 12185.
[12] H. Huang, C. Yu, X. Han, H. Huang, Q. Wei, W. Guo, Z. Wang, J. Qiu, *Energy Environ. Sci.* **2020**, *13*, 4990.
[13] X. Zhao, P. Pachfule, A. Thomas, *Chem. Soc. Rev.* **2021**, *50*, 6871.
[14] J. Du, F. Li, L.-C. Sun, *Chem. Soc. Rev.* **2021**, *50*, 2663.
[15] S. Royuela, E. Martinez-Perinan, M. P. Arrieta, J. I. Martinez, M. M. Ramos, F. Zamora, E. Lorenzo, J. L. Segura, *Chem. Commun.* **2020**, *56*, 1267.
[16] H. Zhu, M. Lu, Y. Wang, S. Yao, M. Zhang, Y. Kan, J. Liu, Y. Chen, S. Liu, Y. Lan, *Nat. Commun.* **2020**, *11*, 497.
[17] J. Liu, D. Yang, Y. Zhou, G. Zhang, G. Xing, Y. Liu, Y. Ma, O. Terasaki, S. Yang, L. Chen, *Angew. Chem., Int. Ed.* **2021**, *60*, 14473.
[18] T. Li, W.-D. Zhang, Y. Liu, Y. Li, C. Cheng, H. Zhu, X. Yan, Z. Li, Z.-G. Gu, *J. Mater. Chem. A* **2019**, *7*, 19676.
[19] B. P. Biswal, S. Chandra, S. Kandambeth, B. Lukose, T. Heine, R. Banerjee, *J. Am. Chem. Soc.* **2013**, *135*, 5328.
[20] L. Wang, Y. Ni, X. Hou, L. Chen, F. Li, J. Chen, *Angew. Chem., Int. Ed.* **2020**, *59*, 22126.

[21] Y. Liao, H. Wang, M. Zhu, A. Thomas, *Adv. Mater.* **2018**, *30*, 1705710.
[22] F. L. Li, Q. Shao, X. Huang, J. P. Lang, *Angew. Chem., Int. Ed.* **2018**, *57*, 1888.
[23] J. Jin, Y. Zheng, S.-z. Huang, P.-p. Sun, N. Srikanth, L. B. Kong, Q. Yan, K. Zhou, *J. Mater. Chem. A* **2019**, *7*, 783.
[24] H. Yang, Q. Lin, C. Zhang, X. Yu, Z. Cheng, G. Li, Q. Hu, X. Ren, Q. Zhang, J. Liu, C. He, *Nat. Commun.* **2020**, *11*, 593.
[25] A. J. Bard, L. R. Faulkner, *Electrochemical Methods Fundamentals and Applications*, John Wiley & Sons, Inc., New York **2001**, pp. 1–850.
[26] D. Chen, S. D. Minteer, *J. Power Sources* **2015**, *284*, 27.
[27] G. Chen, Y. Luo, L. Ding, H. Wang, *ACS Catal.* **2018**, *8*, 526.

ADVANCED FUNCTIONAL MATERIALS

# Supporting Information

for *Adv. Funct. Mater.,* DOI: 10.1002/adfm.202106349

# Molecular Engineering to Tune the Ligand Environment of Atomically Dispersed Nickel for Efficient Alcohol Electrochemical Oxidation

*Zhifu Liang, Daochuan Jiang, Xiang Wang, Mohsen Shakouri, Ting Zhang, Zhongjun Li, Pengyi Tang,* Jordi Llorca, Lijia Liu,* Yupeng Yuan, Marc Heggen, Rafal E. Dunin-Borkowski, Joan R. Morante, Andreu Cabot,* and Jordi Arbiol**

**Molecular Engineering to Tune the Ligand Environment of Atomically Dispersed Nickel for Efficient Alcohol Electrochemical Oxidation**

*Zhifu Liang[+], Daochuan Jiang[+], Xiang Wang, Mohsen Shakouri, Ting Zhang, Zhongjun Li, Pengyi Tang*, Jordi Llorca, Lijia Liu*, Yupeng Yuan, Marc Heggen, Rafal E. Dunin-Borkowski, Joan R. Morante, Andreu Cabot*, Jordi Arbiol**

*Z. F Liang, T. Zhang, Prof. J. Arbiol*

*Catalan Institute of Nanoscience and Nanotechnology (ICN2), CSIC and BIST*

*Campus UAB, Bellaterra, 08193 Barcelona, Catalonia, Spain*

*Email: arbiol@icrea.cat*

*Dr. P. Y Tang*

*Shanghai Institute of Microsystem and Information Technology, Chinese Academy of Sciences, Shanghai 200050, China*

*Email: py.tang@mail.sim.ac.cn*

*Dr. D. Jiang, Prof. Y. Yuan*

*School of Chemistry and Chemical Engineering, Anhui University, Heifei 230601, Anhui Province, China*

*Z.F Liang, X. Wang, Prof. J. R. Morante, Prof. A. Cabot*

*Catalonia Institute for Energy Research - IREC*

*Sant Adrià de Besòs, Barcelona, 08930, Catalonia, Spain*

*Email: acabot@irec.cat*

*Dr. L. Liu*

*Department of Chemistry, Western University, 1151 Richmond Street, London, ON*

*N6A5B7 Canada*

*Email*: *lijia.liu@uwo.ca*

*Dr. P. Y Tang, Dr. M Heggen, Prof. R E. Dunin-Borkowski*

*Ernst Ruska-Centre for Microscopy and Spectroscopy with Electrons and Peter Grünberg Institute Forschungszentrum Jülich GmbH 52425 Jülich, Germany*

*Prof. Z.J Li*

*School of Physics, Hefei University of Technology, Hefei 230009, P. R China*

*Dr. M. Shakouri*

*Canadian Light Source, Saskatoon, S7N 0X4, Canada*

*Prof. J. Llorca*
*Institute of Energy Technologies, Department of Chemical Engineering and Barcelona Research Center in Multiscale Science and Engineering*
*Universitat Politècnica de Catalunya, EEBE, 08019 Barcelona, Catalonia Spain.*

*Prof. A. Cabot, Prof. J. Arbiol*

*ICREA*

*Pg. Lluís Companys 23, 08010 Barcelona, Catalonia, Spain*

[+] These authors contributed equally to this work

* Corresponding authors

**Materials Characterization**

The crystal structure was characterized by means of powder X-ray diffraction (XRD) measured in a Bruker AXS D8 Advance X-ray diffractometer. (Cu-Kα radiation, λ = 1.5106 Å, 40 kV and 40 mA; Bruker, Germany). Thermogravimetric analysis (TGA) were performed under argon gas at a heating rate of 5 °C/min using a Thermogravimetric Analyzer Q200. Scanning electron microscopy (SEM) images were obtained in a Zeiss Auriga field emission scanning electron microscopy (FE-SEM) operating at 20 kV. High angle annular dark-field (HAADF)-scanning transmission electron microscopy (STEM) images and elemental mapping were measured in a spherical aberration corrected transmission electron microscope FEI Titan G2 80-200 ChemiSTEM with four energy-dispersive X-ray spectroscopy (EDX) detectors and operated at 80 and 200 keV. X-ray photoelectron spectroscopy (XPS) data was obtained in a Phoibos 150 MCD-9 detector. Ni K-edge X-ray absorption fine structure (XAFS) spectra were measured at the Canadian Light Source, beamline SXRMB. The samples were pressed onto a double-sided carbon tape and the data was recorded in X-ray fluorescence mode. The XAFS data was processed with the Athena program.[S27] Extended X-ray absorption fine structure (EXAFS) was analyzed using the IFEFFIT package[S28] and the EXAFS fitting was performed with FEFF6L.[S29] For EXAFS fitting, spectra were fitted in R-space, from 1.0 Å to 2.76 Å. The R-space EXAFS signal was obtained by a variable $k^n$-weighted Fourier transform (n = 1, 2, 3) of the EXAFS signal χ(k) over a k-range of 3.00 $Å^{-1}$ to 11.7 $Å^{-1}$. Nitrogen adsorption-desorption isotherms were recorded in a Tristar II 3020 Micromeritics system at 77 K. The specific surface area was calculated by Brunauer–Emmett–Teller (BET) methods.

**Electrochemical Measurements**

All the electrochemical measurements were carried out on the Chi760 electrochemical workstation (Shanghai Chenhua, China) at room temperature by using a standard three-electrode setup system without iR compensation. A platinum grid, glassy carbon electrode with 5 mm diameter and Hg/HgO electrode were used as counter electrode, working electrode and reference electrode, respectively. 4 mg of Ni-2D-O-SA-CNT (or

Ni-2D-SA-CNT) catalysts and 30 μL of 10% Nafion solution were added to 75 μL isopropanol and 425 μL MiliQ water, then the obtained solution was sonicated for half an hour to obtain a homogeneous solution. 10 μL mixture solution was dropped on the working electrode for drying before the electrochemical tests. All the tests were performed in argon-bubbled 1 M KOH solution with or without alcohol and with magnetic stirring. Linear sweep voltammetry (LSV) curve measurements were conducted in 1.0 M KOH at room temperature with and without 1 M methanol, 1 M ethanol and 0.1 M benzyl alcohol solution, respectively. For oxygen evolution reaction (OER), methanol oxidation reaction (MOR), Ethanol Oxidation Reaction (EOR) and benzyl alcohol oxidation reaction (BOR), the scan rate of LSV curves was 5 mV $s^{-1}$. The solution resistance estimated from electrochemical impedance spectroscopy (EIS) measurements was recorded under alternating current voltage with frequencies from 0.01 to $10^5$ Hz. $^1$H NMR spectra was recorded on an AVANCE III console (Bruker). In which 1 mL electrolyte was added with 200 μL $D_2O$.

**Calculation Details**

All calculations presented were carried out for the selected fragments using the density functional theory (DFT) with the generalized Perdew-Burke-Ernzerhof (PBE), and the projector augmented-wave (PAW) pseudopotential planewave method as implemented in the VASP code. [S30, S31] DFT-D3 correction method was employed to describe van der Waals interaction. The cutoff energy of plane-wave basis was 500 eV. The convergence of energy was set as $10^{-5}$ eV. A 1 × 1 × 1 k-point mesh was used for the Brillouin Zone sampling. A vacuum region of 15 Å was set between adjacent layers to avoid artificial interactions. The selected fragments for Ni-2D-SA and Ni-2D-O-SA consisting of 66 atoms are shown in **Figure S14**. During the structure optimization, all atoms of the selected fragments are fully relaxed until the force on each of the atoms is less than 0.02 eV $Å^{-1}$. In order to investigate the adsorption behavior of methanol molecule on the surface of the selected fragment, a single methanol molecule was placed near the potential adsorption sites of the fragments, and adsorption energy ($E_{ads}$) is defined as $E_{ads} = E_{(methanol+slab)} - E_{slab} - E_{methanol,}$ where $E_{slab}$ is the energy for the

selected fragment, and $E_{(methanol+slab)}$ is the total energy for methanol adsorbed selected fragment.

## Experimental Section

### Materials

Dichloromethane (99%), methanol (99%), N,N-dimethylformamide (DMF, 98%), and hydrazine hydrate (98%) were purchased from Alfa Aesar. Tetrachloro-p-benzoquinone (99%), potassium phthalimide (98%), N-methyl-pyrrolidone (NMP, 99.99%), 2,5-dimethoxyterephthalaldehyde (97%), 1,2,4,5-benzenetetraamine tetrahydrochloride (TAB), hexane (95%), boron tribromide (99.99%), and Nafion (10%) were purchased from Sigma-Aldrich. Benzyl alcohol (99%), nickel acetate tetrahydrate (99%), potassium hydroxide (85%, Acros Organics), acetonitrile (98%) and ethanol (99.5%), were purchased from Honeywell. Carbon Nanotubes were purchased from Sailing Tech company in Shenzhen, China. All chemicals were used without further purification.

### Synthesis of 2,5-dihydroxyterephthalaldehyde (HBC)

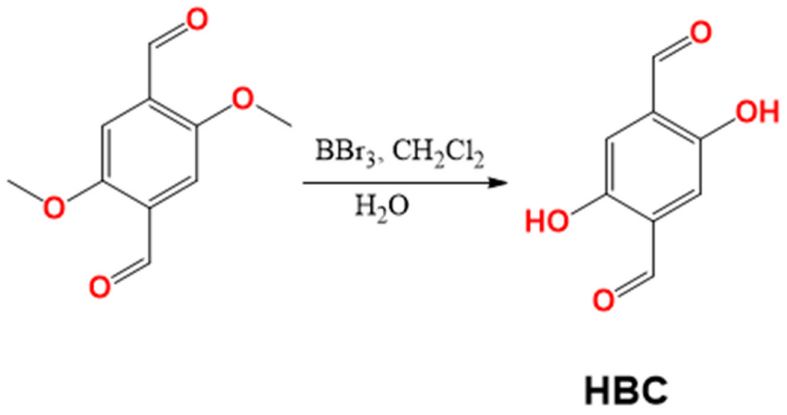


Scheme S1. The synthesis of HBC

2,5-dimethoxyterephthalaldehyde (250 mg, 1.285 mmol) and 25 mL dichloromethane were added to a 50 mL round bottom flask and stirred for 10 min. Then, 3.22 mL BBr3 (1M in hexane) was added to the solution dropwise. After stirring for 3 hours at room temperature, 5 mL water was added dropwise. Solvents were then removed by argon flow, and the resulting solid was filtrated and washed first with water, and then with

acetone to obtain a bright yellow compound, 2,5-hydroxyterephthalaldehyde (HBC) (160 mg, 0.96 mmol, yield 75%). (IR O-H:3260 $cm^{-1}$, -CHO: 2881, -C=O: 1664 cm-1) $^1$H-NMR (400 MHz, DMSO-$d_6$, δ): δ 10.33 (m, 4H), 7.25 (s, 2H). [S1]

**Synthesis of Tetramino-benzenequinone (TABQ)**

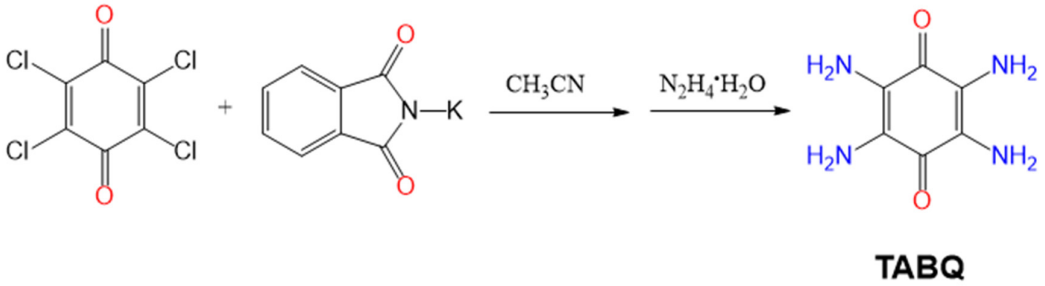


TABQ

Scheme S2. The synthesis of TABQ

5.0 g of tetrachloro-p-benzoquinone and 15.0 g of potassium phthalimide were added to 50.0 mL of acetonitrile under argon and then stirred at 80 ℃ for 12 h. After cooling to room temperature, the products were filtered, and washed with DMF, hot deionized water and ethanol for several times and then vacuum filtered. It was then dried in a vacuum oven at 60 ℃ for 12 h. 10.0 g (yield 71.0%) brown-yellow of tetra(phthalimido)-benzoquinone was obtained.[S2] The obtained tetra(phthalimido)-benzoquinone was put into a 100 mL round bottom flask, then 40.0 mL of hydrazine hydrate (98%) was added. After maintained at 65 ℃ for 2 h, purple tetramino-benzoquinone (TABQ) (1.8 g, yield 26.0%) was obtained. (IR -NH2: 3367 $cm^{-1}$, -C=O: 1668 cm-1, C-(C=O)-C 1140 $cm^{-1}$) $^1$H-NMR (400 MHz, DMSO-$d_6$, δ): δ 4.55 (s, 8H). [S3-S4]

**Synthesis of Ni-2D-O-SA**

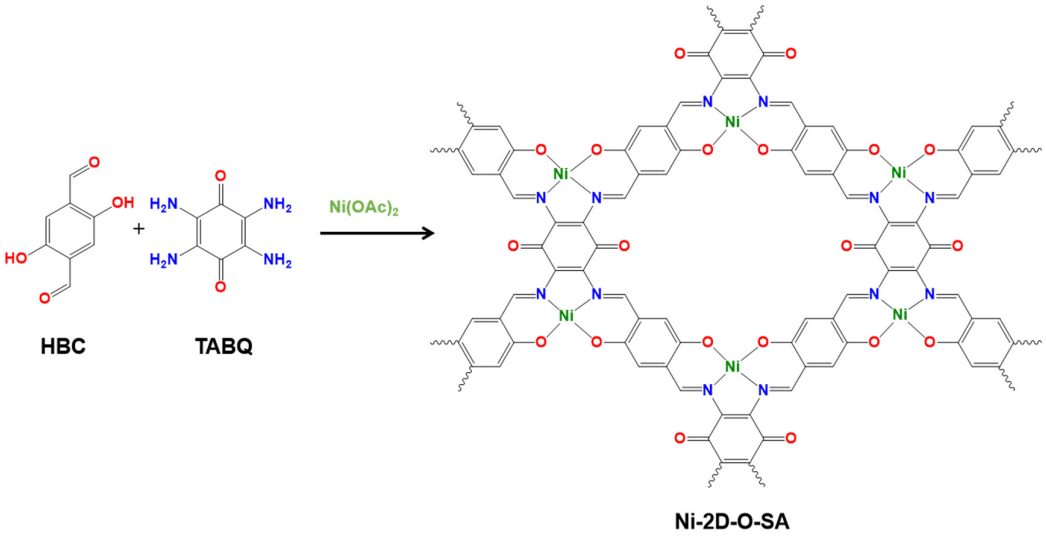


Scheme S3. The synthesis of Ni-2D-O-SA

2,5-hydroxyterephthalaldehyde (HBC) (166 mg, 1 mmol) and TABQ (84 mg, 0.5 mmol), excess nickel acetate, and 5 mL dried NMP were added to a 10 mL glass bottle. The resulting solution was sonicated for half an hour to obtain a homogenous dispersion. The glass bottle was transferred into a 25 mL Teflon-lined stainless-steel autoclave. The autoclave was sealed and kept at 120 ºC for 72 h and cooled to room temperature. The resulting black precipitate was collected by filtration and washed with DMF and methanol, Soxhlet extracted by methanol for 24 h, then vacuum dried at 60 ºC for 24 h to give a black powder with ~83% yield ($C_{11}N_2O_3NiH_4 \cdot 2H_2O$, Elemental Analysis, Calculated: C, 43.05 %; H, 2.63 %; N, 9.13 %; Found: C, 42.04 %; H, 3.14 %; N, 8.36 %).

**Synthesis of Ni-2D--SA**

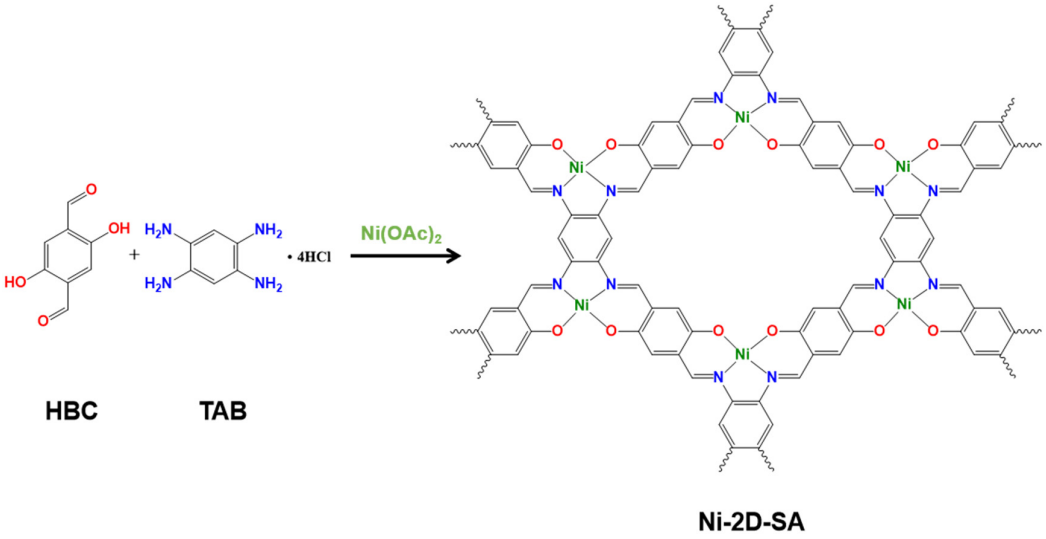


Scheme S4. The synthesis of Ni-2D-SA

The synthesis procedure of Ni-2D-SA is similar as Ni-2D-O-SA, just using 1,2,4,5-benzenetetraamine tetrahydrochloride (TAB) to replace TABQ ($C_{11}N_2O_2NiH_5 \cdot H_2O$ elemental analysis Calculated: C, 48.24 %; H, 2.58 %; N, 10.23 %; Found: C %, 47.34 %; H, 3.24 %; N, 9.26 %).[S5]

**Pre-oxidation of Carbon Nanotubes (CNT)[S33]**

The purchased CNTs were annealed at 500 ℃ in air for 5 h. After cooling to room temperature, the CNTs were added to a 20 mL 5 wt% HCl aqueous solution and sonicated for 30 min. The pre-oxided CNTs were collected by vacuum filtration and washed extensively with MILIQ water for several times and dried at 60℃ for 12 h.

**Synthesis of Ni-2D-O-SA/CNT composites**

30 mg Ni-2D-O-SA and 70 mg pre-oxidized carbon nanotube were put into a 15 mL glass vial, then 5 mL NMP was added. The resulting solution was sonicated for half an hour, and stirred at 100 ℃ for 12 h. The resulting black composite was collected by

filtration and washed with ethanol, then vacuum dried at 60 ℃ for 24 h to obtain the final composite.

**Synthesis of Ni-2D-SA/CNT composites**

Ni-2D-SA/CNT composites were prepared by using the same method as for Ni-2D-O-SA/CNT, just using Ni-2D-SA to replace Ni-2D-O-SA.

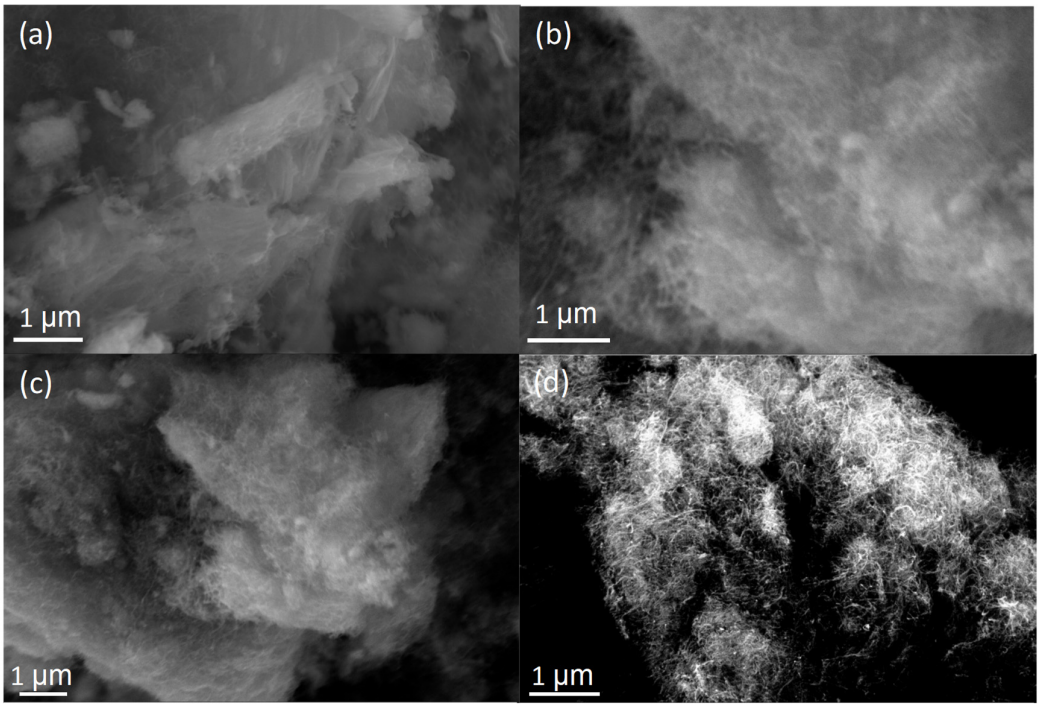


Figure S1. SEM images of Ni-2D-O-SA (a,b); Ni-2D-O-SA-CNT (c); Ni-2D-SA-CNT (d).

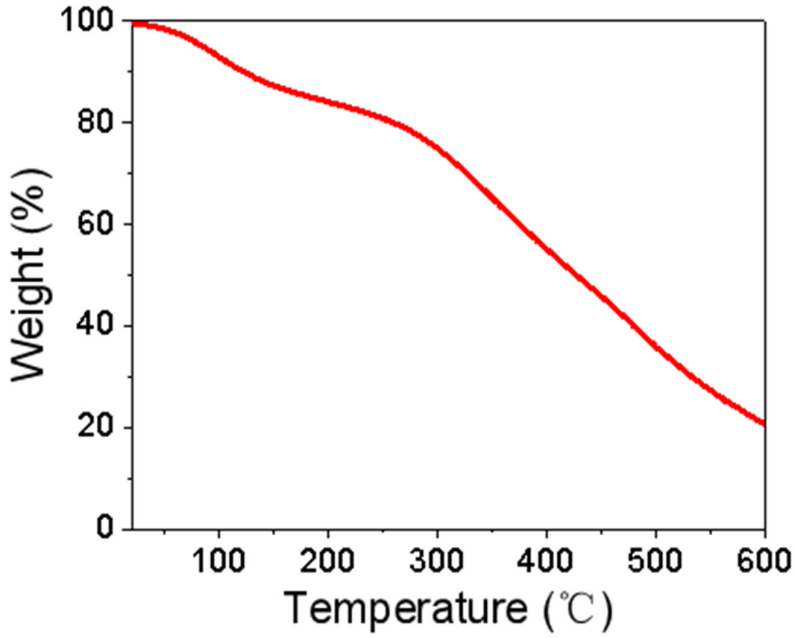


**Figure S2.** TGA of Ni-2D-O-SA under argon by heating to 600 ℃ at the rate of 5 ℃/min.

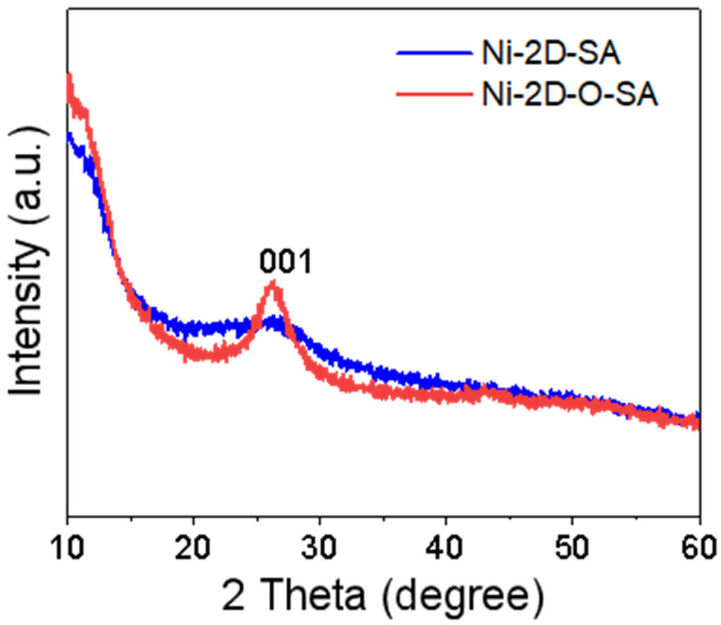

Figure S3. XRD patterns of Ni-2D-SA (blue) and Ni-2D-O-SA (red)

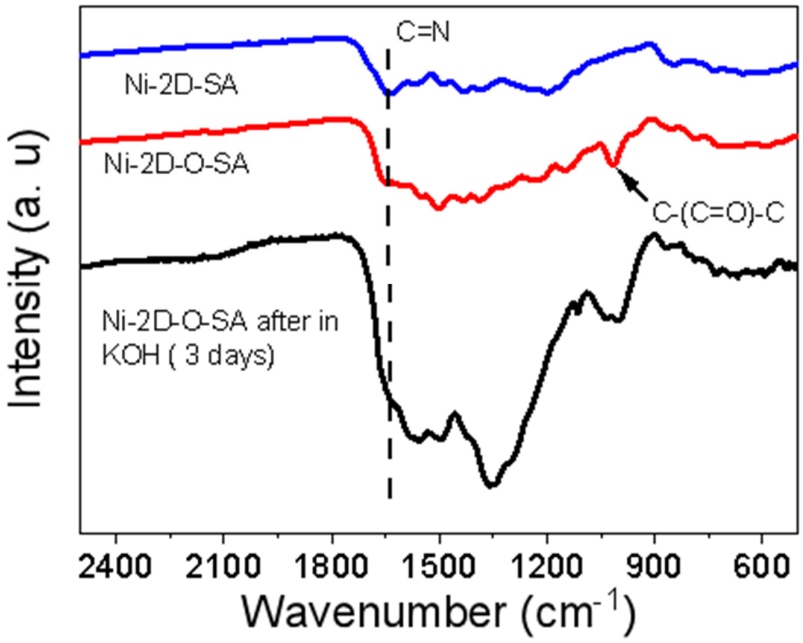


Figure S4. FT-IR spectra of Ni-2D-SA and Ni-2D-O-SA

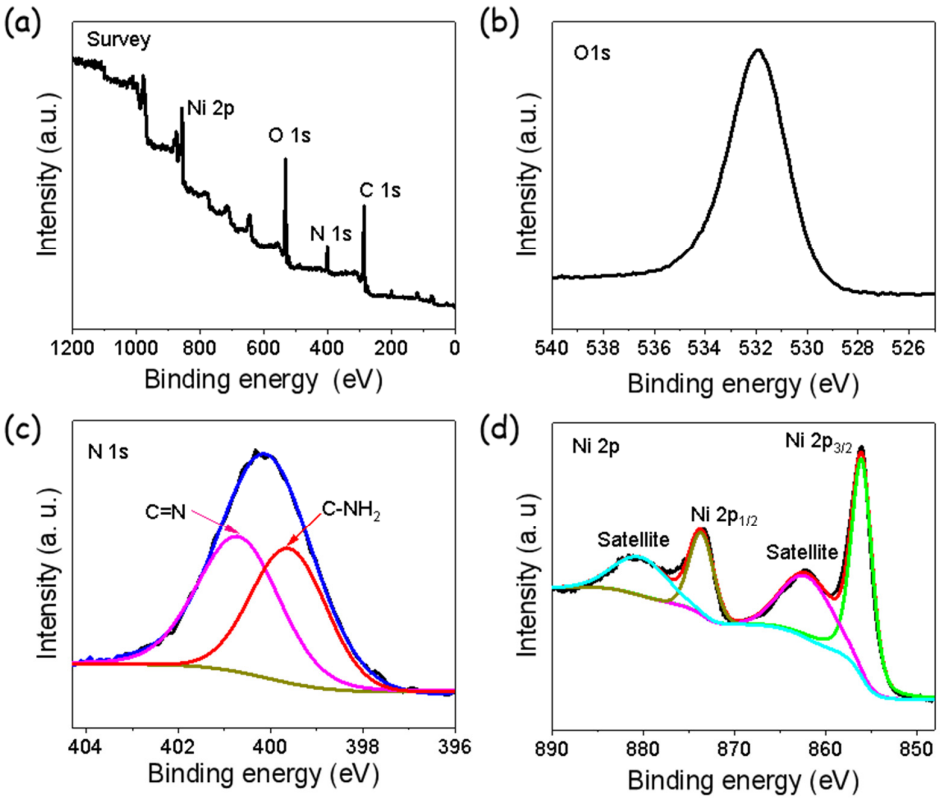


Figure S5. (a) Survey, (b-d) high-resolution O 1s, N 1s, and Ni 2p XPS spectra of Ni-2D-O-SA

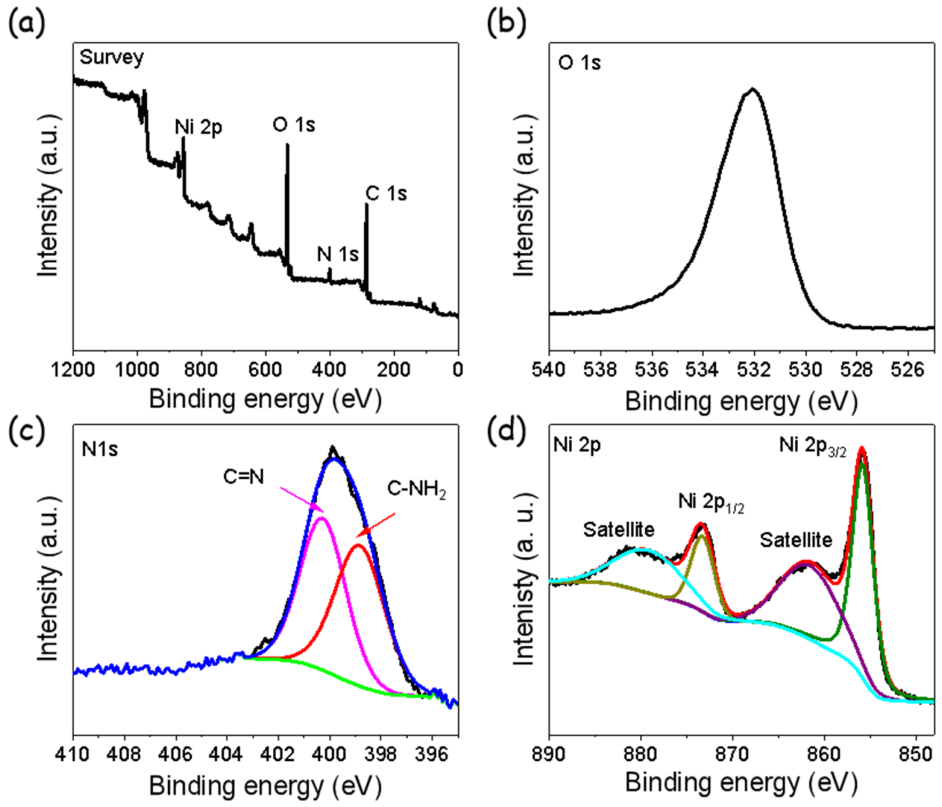


Figure S6. (a) Survey, (b-d) high-resolution O 1s, N 1s, and Ni 2p XPS spectra of Ni-2D-SA

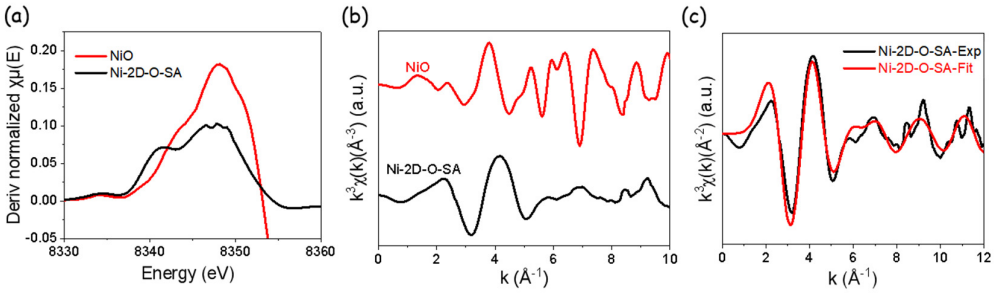


Figure S7. Ni K-edge EXAFS oscillations in k-space ($k^3\chi(k)$) of Ni-2D-O-SA and its fitted spectrum.

**Table S1.** Ni K-edge EXAFS fitting parameters for Ni-2D-O-SA

| sample | Bond | R(Å) | CN | $\sigma^2$ ($10^{-3}$ Å$^2$) | ΔE (eV) | R factor |
|---|---|---|---|---|---|---|
| Ni-2D-O-SA | Ni-O | 1.87 | 2 | 4.7 | -3.60 | 0.03 |
| | Ni-N | 2.05 | 2 | 1.4 | | |
| | Ni...C | 2.65 | 6 | 5.8 | | |

R：bond length, CN: coordination number

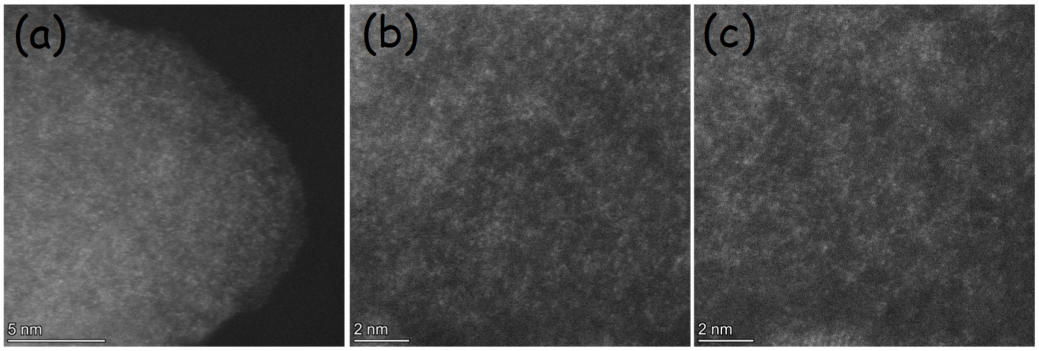


Figure S8. (a)-(c) HAADF-STEM images of Ni-2D-O-SA displaying the presence of atomically dispersed nickel atoms. (d) Low magnification HAADF-STEM images.

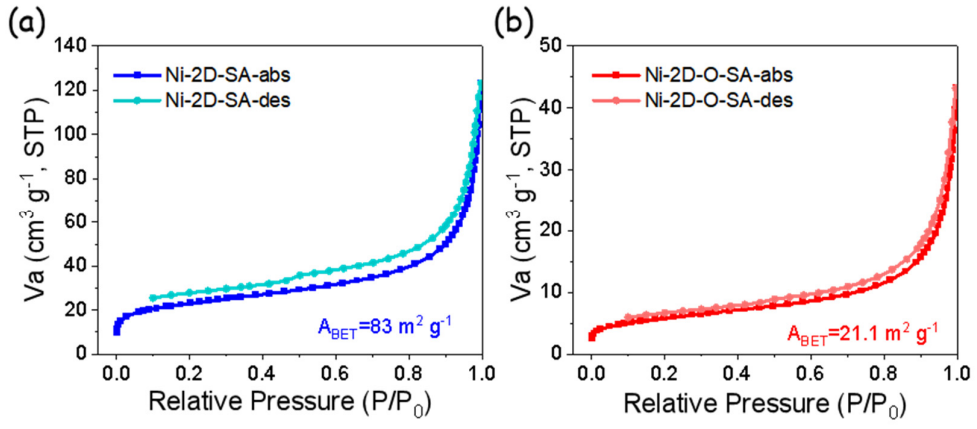


Figure S9. $N_2$ adsorption-desorption isotherm of (a) Ni-2D-SA and (b) Ni-2D-O-SA.

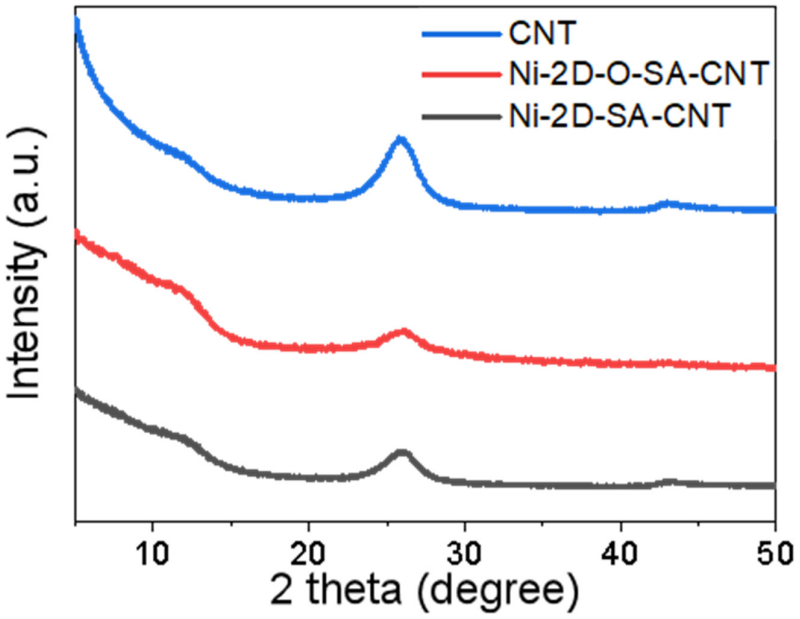


Figure S10 XRD patterns of Ni-2D-SA-CNT, Ni-2D-O-SA-CNT and CNT

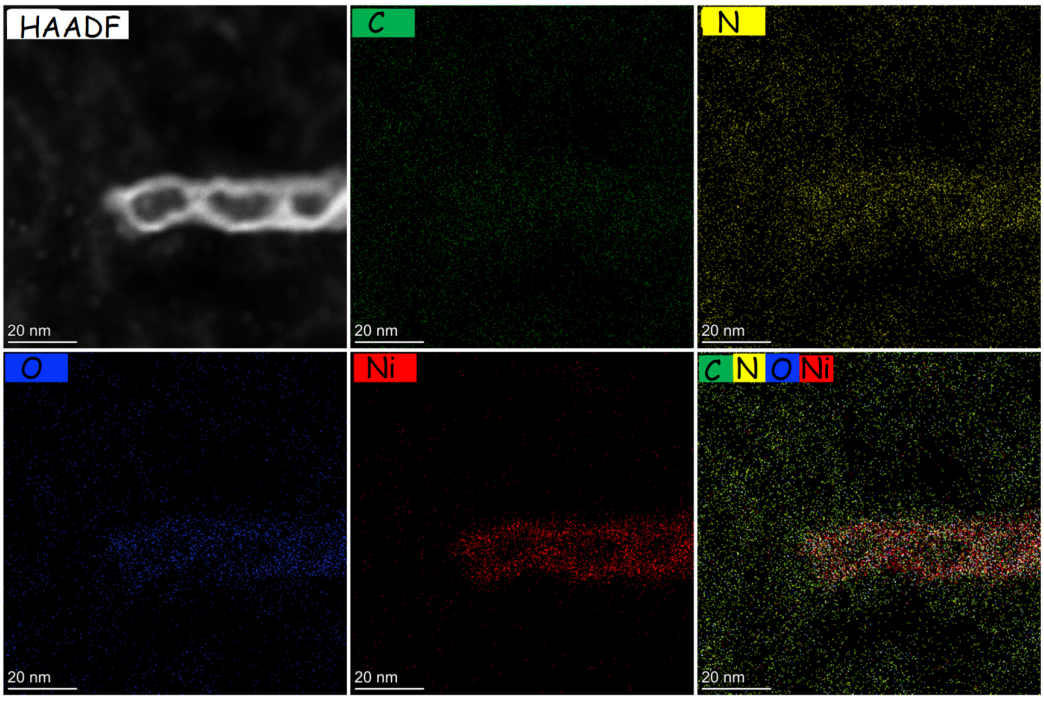


Figure S11. Low magnification HAADF-STEM image and EDS elemental maps of the Ni-2D-O-SA-CNT sample.

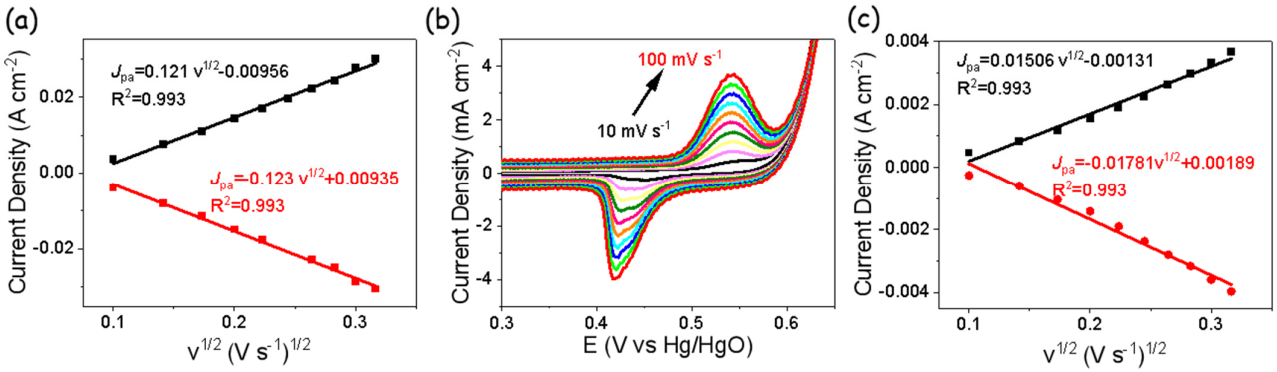


Figure S12 (a) Linear fitting of the anodic and cathodic peak current densities to the square root of the sweep rate for Ni-2D-O-SA-CNT. (b) Cyclic voltammograms of Ni-2D-SA-CNT electrocatalysts in 1 M KOH with increasing potential sweep rate from 10 to 100 mV $s^{-1}$. (c) Linear fitting of the anodic and cathodic peak current densities to the square root of the sweep rates for Ni-2D-SA-CNT.

The surface coverage of $Ni^{2+}/Ni^{3+}$ in these two catalysts was investigated by the following equation.[S6-S7]

$$\Gamma = \frac{Q}{nFA} \qquad \text{(equation S1)}$$

Where $Q$ is the charge from the reduction/oxidation peak, calculated from the average of forward and reverse scan, $n$ is the number of electrons, $F$ is the Faraday constant and $A$ is working geometrical electrode surface area.

Figure S14a and Figure S14c display the good linear relationship of the anodic and the cathodic peak current density of the Ni-2D-O-SA-CNT and Ni-2D-SA-CNT electrode vs the square root of the scan rate. The diffusion coefficient ($D$) is an important parameter to evaluate the oxidation behavior of electrocatalyst. Normally $D$ was calculated by the following equation:[S32]

$$I_p = 2.69\times10^5 n^{3/2} A D^{1/2} C v^{1/2} \qquad \text{(equation S2)}$$

Where $I_p$ is the peak current, $n$ is the number of transferred electron, $A$ is apparent area

of electrode, $D$ is the diffusion coefficient, $C$ is the initial concentration of redox species. $v$ is the scan rate.

And here we definite a apparent diffusion coefficient ( $D'$ ):

$$D' = D^{1/2} C \qquad \text{(equation S3)}$$

So the apparent coefficient $D'$ was calculated by the following equation:

$$I_p = 2.69 \times 10^5 n^{3/2} A D' v^{1/2} \qquad \text{(equation S4)}$$

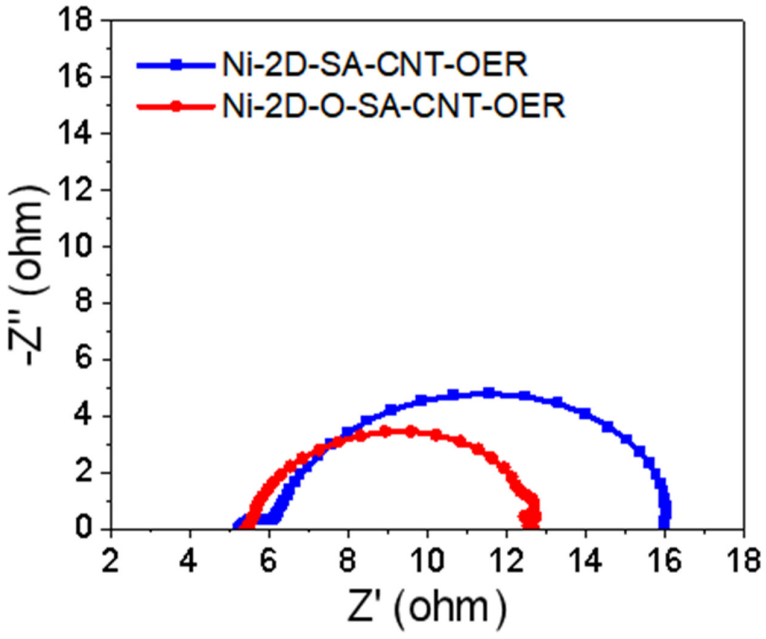


Figure S13. EIS spectra of the two catalysts at 0.67 V vs Hg/HgO in 1 M KOH solution.

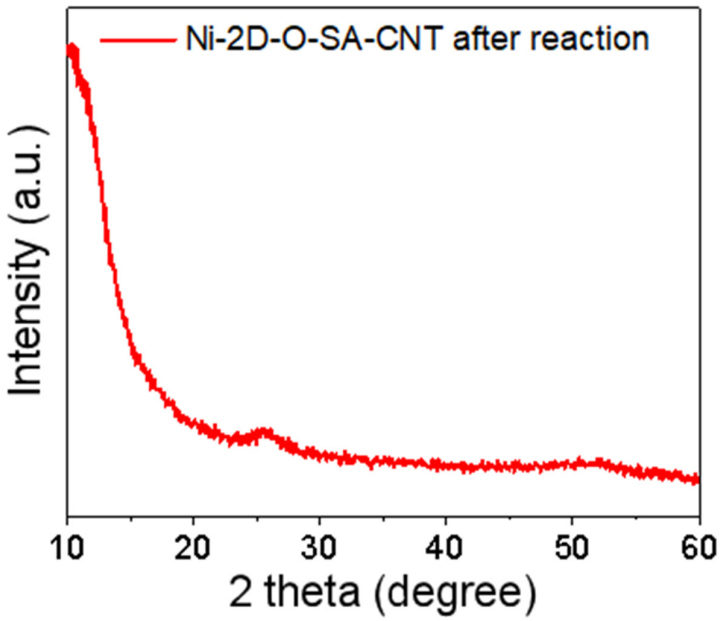


Figure S14. XRD pattern of Ni-2D-O-SA-CNT after MOR electrochemical experiments.

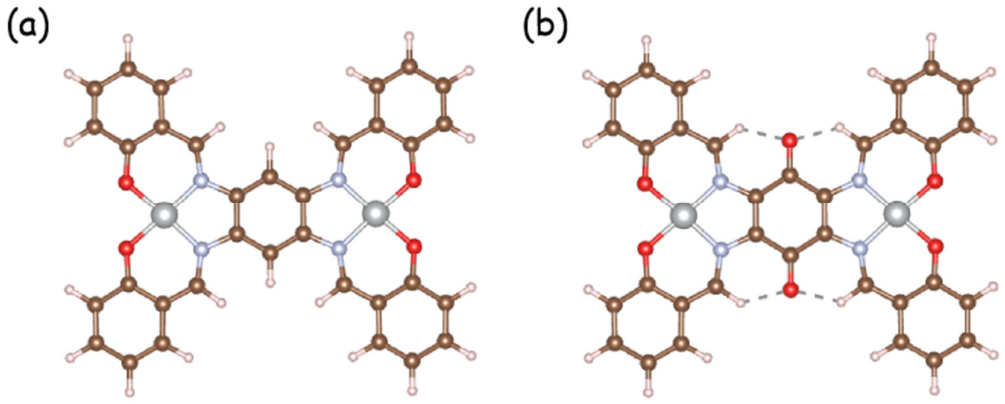


Figure S15. Selected fragment of Ni-2D-SA (a) and Ni-2D-O-SA (b).

**Table S2.** Summary of the DFT calculation results for methanol adsorption: adsorption energy and distance with Ni and C=O chemical group.

| Sample | Adsorption energy (eV) with Ni | Adsorption distance (Å) with Ni | Adsorption distance (Å) with C=O |
|---|---|---|---|
| Ni-2D-SA | -0.225 | 3.11 | 2.5 |
| Ni-2D-O-SA | -0.248 | 3.27 | 1.87 |

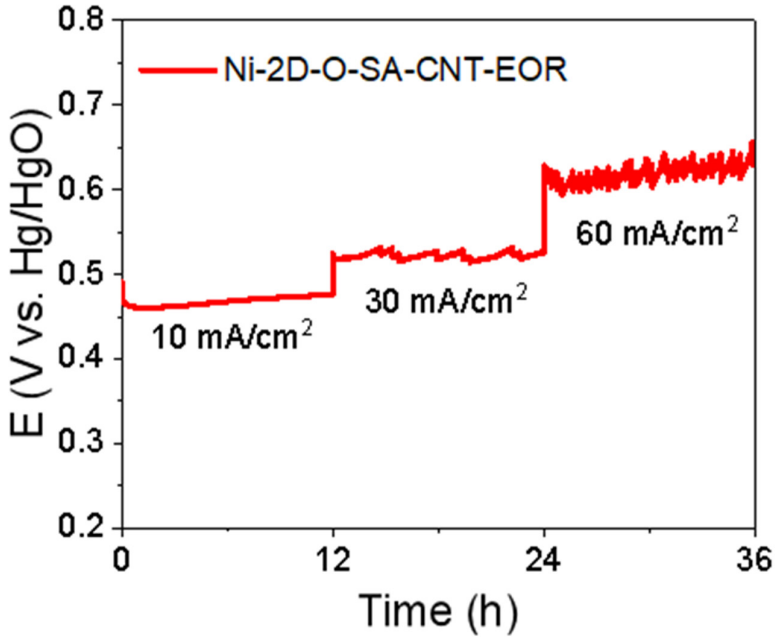


Figure S16. CP data showing the long term EOR stability of Ni-2D-O-SA-CNT at 10 mA/cm$^2$, 30 mA/cm$^2$ and 60 mA/cm$^2$.

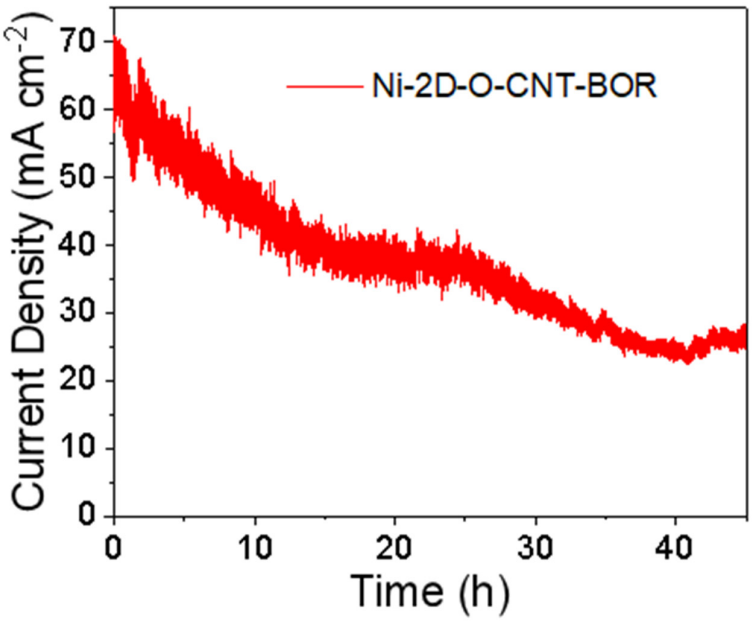


Figure S17. *i-t* curve of Ni-2D-O-SA-CNT at 0.55 V vs Hg/HgO.

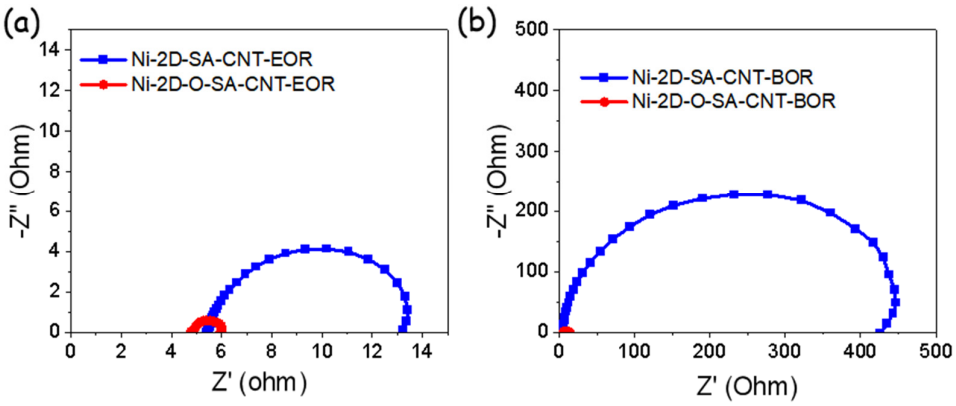


Figure S18. (a) EIS spectrum at 0.60 V in 1 M KOH+1M ethanol solution. (b) EIS at 0.50 V in 1 M KOH+0.1 M benzyl alcohol solution.

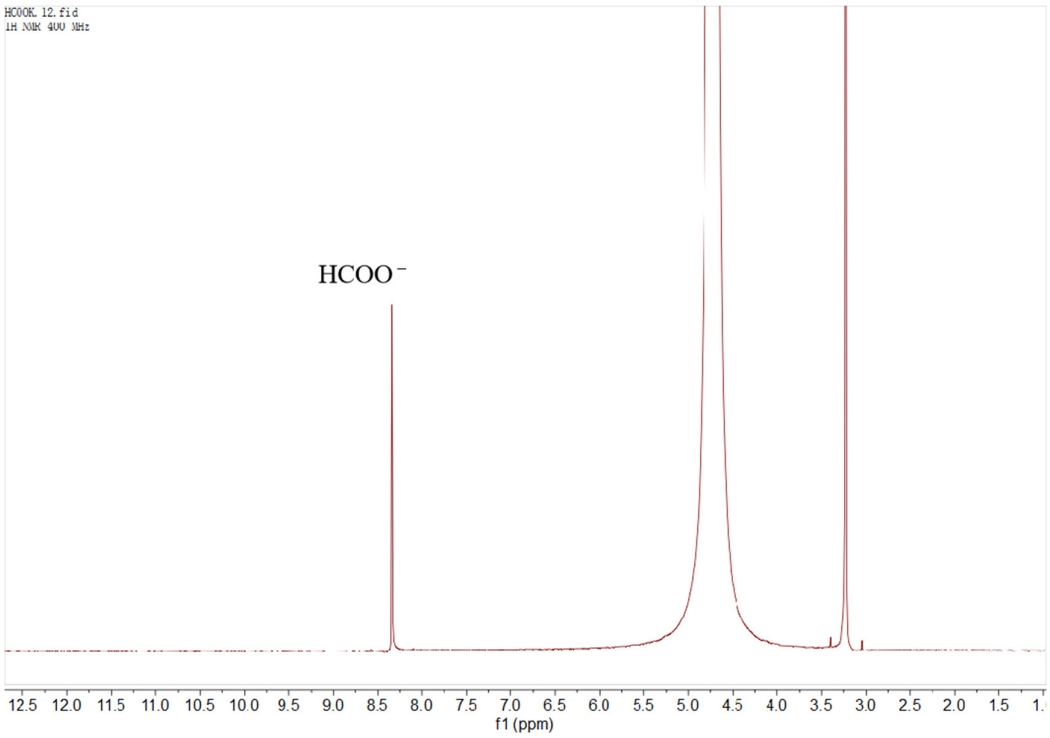


Figure S19. $^{1}$H NMR spectra of methanol electrochemical oxidation on Ni-2D-O-SA-CNT electrode after 36 h stability test.

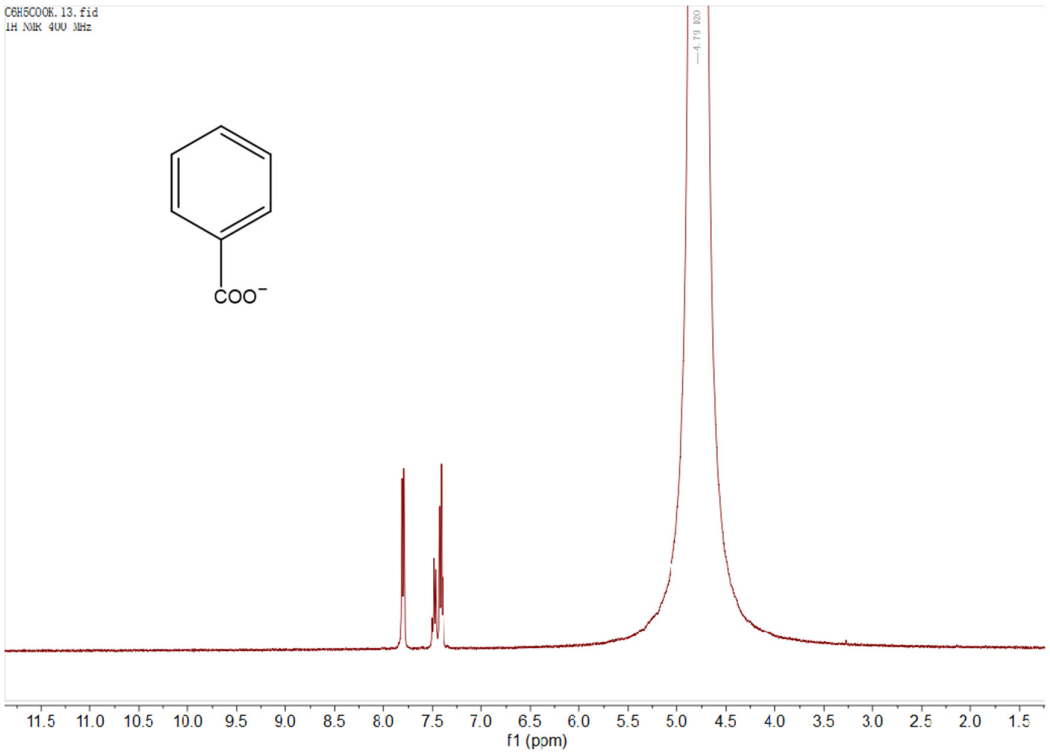

Figure S20. $^{1}$H NMR spectra of benzyl alcohol electrochemical oxidation on Ni-2D-O-SA-CNT electrode after at 0.55 V vs HgO/Hg until the current close to zero.

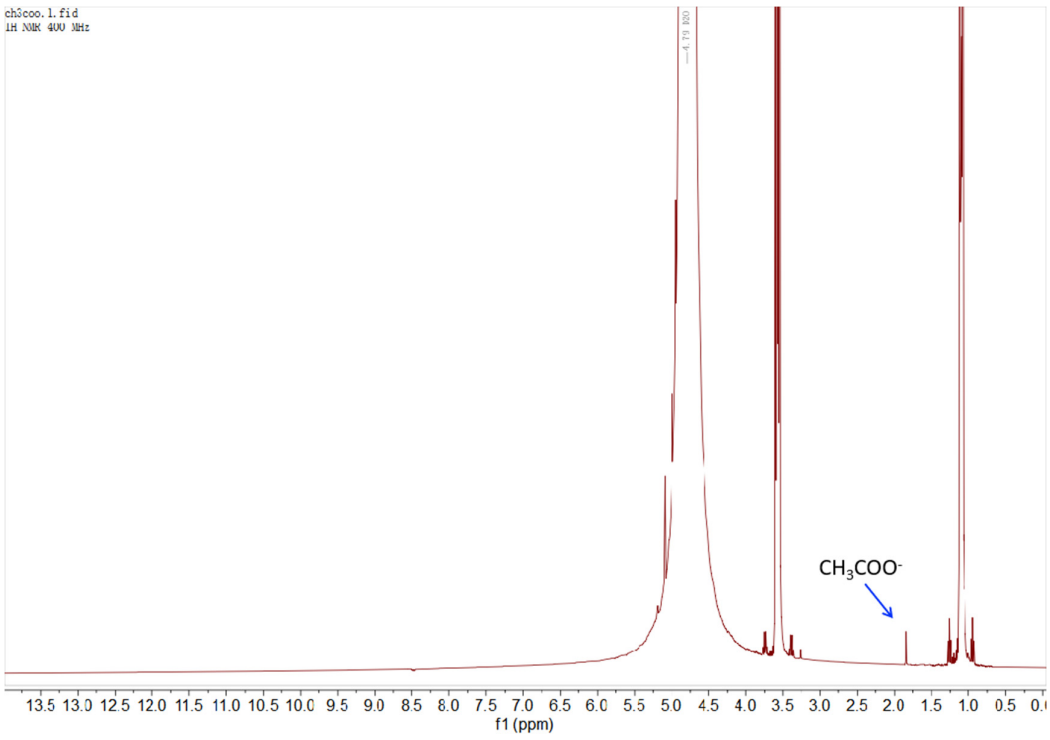


Figure S21. $^{1}$H NMR spectra of ethanol electrochemical oxidation on Ni-2D-O-SA-CNT electrode after 12 h stability test at 0.7 V vs HgO/Hg.

**Table S3.** Summary of the catalytic performance for MOR and EOR in alkaline solution

| Catalysts | Current density ($mA\ cm^{-2}$) | Electrolyte | References |
|---|---|---|---|
| **Ni-2D-O-SA-CNT** | **106[a]** | **1.0 M KOH + 1.0 M methanol** | **This work** |
| $Ni_{0.75}Cu_{0.25}$ | 84 | 1.0 M NaOH + 0.5 M methanol | [S8] |
| Ni NCs | 61 | 1.0 M KOH + 1.0 M methanol | [S9] |
| $Ni_{2.5}Co_{0.5}Sn_2$ | 65.5 | 1.0 M KOH + 1.0 M methanol | [S10] |
| Cu/NiCu NWs-220/C | 34.9 | 1.0 M KOH + 1.0 M methanol | [S11] |
| Ni/CN | 27 (under visible light) | 1.0 M KOH + 3.0 M methanol | [S12] |
| NiCo/NiO-CoO/NPCC/GCE | 178 | 0.5 M NaOH + 0.5 M methanol | [S13] |
| NiO@C/CC | 188.6 | 1.0 M KOH + 1.0 M methanol | [S14] |
| KB&CTGU-15(1:2) | 29.8 | 0.1 M KOH + 1.0 M methanol | [S15] |
| **Ni-2D-O-SA-CNT** | **101[a]** | **1.0 M KOH + 1.0 M ethanol** | **This work** |
| Ni-NPs | 47 | 1.0 M KOH + 1.0 M ethanol | [S16] |

| | | | |
|---|---|---|---|
| $Ni_xCo_{1-x}$ alloy | 142 | 1.0 M KOH + 5.0 M ethanol | [S17] |
| $Co_{0.2}Ni_{0.2}$ | 75 | 1.0 M KOH + 1.0 M ethanol | [S18] |
| Hierachical $TiO_2$/ZnO | 25 | 1.0 M KOH + 1.0 M ethanol | [S19] |
| NiNC-4 | 327 | 0.1 M NaOH + 1.0 M ethanol | [S20] |
| NiO@C/CC | 119.1 | 1 M KOH + 1.0 M ethanol | [S14] |
| Ni-B NTs | 19.2 | 0.1 M NaOH + 0.5 M ethanol | [S21] |
| NiNC-3 | 71.22 | 0.1 M NaOH + 1.0 M ethanol | [S22] |
| Ni/aHC | 55 | 1.0 M NaOH + 1.0 M ethanol | [S23] |

[a] The calculation is calculated before appearance of the competition reaction OER.

**Table S4.** Summary of the catalytic performance for benzyl alcohol (BA) electrochemical oxidation (BOR) in alkaline solution from recent reports

| Catalysts | Current density (mA $cm^{-2}$) | Mass activity (mA $mg^{-1}$) | Electrolyte | Reference |
|---|---|---|---|---|
| **Ni-2D-O-SA-CNT** | **77[a]** | **1020** | **0.1 M BA** | **This work** |
| $Co_3O_4$ NWs/Ti | 2 | / | 10 mM BA | [S24] |
| NC@CuCo2Nx/CF | 25 | / | 15 mM BA | [S25] |
| A-Ni-Co-H/NF | 400 | / | 0.1 M BA | [S26] |

[a] Calculated before appearance of the competing OER.

## References


[S1] S. J. Lyle, T. M. Osborn Popp, P. J.Waller, X. Pei, J. A. Reimer, O. M. Yaghi, *J. Am. Chem. Soc* **2019**, 141, 28, 11253–11258.

[S2] Kurt A.W. Wallenfels, Wilfried J. Draber, *Tet. Lett* **1959**, 667, 55

[S3] Manivannan, R.; Ciattini, S.; Kuppanagounder, L. C.; Elango, P., *RSC Adv* **2015**, 5, 87341.

[S4] Stang, S.; Lebkücher, A.; Walter, P.; Kaifer, E.; Himmel, H. J.; *Eur. J. Inorg. Chem*. **2012**, 4833.

[S5] T. Li, W.-D. Zhang, Y. Liu, Y. Li, C. Cheng, H. Zhu, X. Yan, Z. Li, Z.-G. Gu, *Journal of Materials Chemistry A* **2019**, *7*, 19676-19681.

[S6] A. J. Bard, L. R. Faulkner, *Electrochemical Methods Fundamentals and applications* **2001**.

[S7] D. Chen, S. D. Minteer, *Journal of Power Sources* **2015**, *284*, 27-37.

[S8] X. Cui, P. Xiao, J. Wang, M. Zhou, W. Guo, Y. Yang, Y. He, Z. Wang, Y. Yang, Y. Zhang, Z. Lin, *Angew Chem Int Ed Engl* **2017**, *56*, 4488-4493.

[S9] J. S. Li, Y. Zuo, J. F. Liu, X. Wang, X. T. Yu, R. F. Du, T. Zhang, M. F. Infante-Carrió, P. Y. Tang, J. Arbiol, J. Llorca, Z. S. Luo, A. Cabot, *J. Mater. Chem. A* **2019**, 7, 22036.

[S10] J. Li, Z. Luo, F. He, Y. Zuo, C. Zhang, J. Liu, X. Yu, R. Du, T. Zhang, M. F. Infante-Carrió, P. Tang, J. Arbiol, J. Llorca, A. Cabot, *J. Mater. Chem. A* **2018**, 6, 22915

[S11] D. F. Wu, W. Zhang, D. J. Cheng, *ACS Appl. Mater. Interfaces* **2017**, 9, 19843

[S12] I. S. Pieta, A. Rathi, P. Pieta, R. Nowakowski, M. Hołdynski, M. Pisarek, A. Kaminska, M. B. Gawande, R. Zboril, *Appl. Catal*. *B* **2019**, 244, 272.

[S13] S. Rezaee, S. Shahrokhian, *Appl. Catal. B* **2019**, 244, 802.

[S14] C. Liu, W. Zhou, J. Zhang, Z. Chen, S. Liu, Y. Zhang, J. Yang, L. Xu, W. Hu, Y. Chen, Y. Deng, *Advanced Energy Materials* **2020**, *10*.

[S15] Y. Wu, J. Tian, S. Liu, B. Li, J. Zhao, L. Ma, D. Li ,Y. Lan, X. Bu, *Angew Chem Int Ed Engl* **2019**, *58*, 12185-112189

[S16] N. A. M. Barakat, H. M. Moustafa, M. M. Nassar, M. A. Abdelkareem, M. S. Mahmoud, A. A. Almajid, K. A. Khalil, *Electrochim. Acta* **2015**, 182, 143.

[S17] N. A. M. Barakat, M. Motlak, A. A. Elzatahry, K. A. Khalil, E. A. M. Abdelghani, Int. J. Hydrogen Energy 2014, 39, 305

.[S18] N. A. M. Barakat, M. Motlak, B. H. Lim, M. H. El-Newehy, S. S. Al-Deyab, *J. Electrochem. Soc.* **2014**, 161, F1194

[S19] G. M. K. Tolba, N. A. M. Barakat, A. M. Bastaweesy, E. A. Ashour, W. Abdelmoez, M. H. El-Newehy, S. S. Al-Deyab, H. Y. Kim, *Journal of Materials Science & Technology* **2015**, *31*, 97-105.

[S20] W. J. Shi, Q. Wang, F. M. Qin, J. G. Yu, M. M. Jia, H. Y. Gao, Y. B. Zhang, Y. N. Zhao, G. D. Li, *Electrochim. Acta* **2017**, 232, 332.

[S21] F. Muench, M. Oezaslan, M. Rauber, S. Kaserer, A. Fuchs, E. Mankel, J. Brötz, P. Strasser, C. Roth, W. Ensinger, *J. Power Sources **2013***, 222, 243.

[S22] W. J. Shi, H. Y. Gao, J. G. Yu, M. M. Jia, T. M. Dai, Y. N. Zhao, J. J. Xu, G. D. Li, *Electrochim. Acta* **2016**, 220, 486.

[S23] A. Cuña, C. Reyes Plascencia, E. L. da Silva, J. Marcuzzo, S. Khan, N.Tancredi,M. R. Baldan, C. de Fraga Malfatti, *Appl. Catal. B* **2017**, 202, 95.

[S24] J. Zheng, X. Chen, X. Zhong, S. Li, T. Liu, G. Zhuang, X. Li, S. Deng, D. Mei, J.-G. Wang, *Adv. Fun. Mater* **2017**, 27, 1704169.

[S25] Z. Yin, Y. Zheng, H. Wang, J. Li, Q. Zhu, Y. Wang, N. Ma, G. Hu, B. He, A. Knop-Gericke, R. Schlogl, D. Ma, *ACS Nano* **2017**, 11, 12365–12377

[S26] H. Huang, C. Yu, X. Han, H. Huang, Q. Wei, W. Guo, Z. Wang, J. Qiu, *Energy & Environmental Science* **2020**, 13, 4990-4999.

[S27] B. Ravel, M. Newville, *J. Synchrotron Rad.* **2005**,12, 537–541.

[S28] M. Newville, *J. Synchrotron Rad.* **2001**, 8, 322–324.

[S29] J. J. Rehr, J. Mustre de Leon, S. I. Zabinsky, R. C. Albers, *J. Am. Chem. Soc.* **1991**, 113, 5135–5140.

[S30] G. Kresse, J. Furthmüller. Comput. Mater. Sci. 1996, 6, 15-50.

[S31] G. Kresse, J. Furthmüller. Phys. Rev. B: Condens. Matter. 1996, 54, 11169.

[S32] A. J. Bard, L. R. Faulkner, *Electrochemical Methods Fundamentals and applications* **2001**.

[S33] Y. Wu, Z. Jiang, X. Lu, et al. Nature **2019**, 575, 639-642.